

Research Article

Thi Doan-Tan, Xuan-Huy Nguyen, and Phe Van Pham*

A new finite element formulation for the lateral torsional buckling analyses of orthotropic FRP-externally bonded steel beams

<https://doi.org/10.1515/cls-2024-0011>

received April 18, 2024; accepted August 05, 2024

Abstract: The present study develops a new finite element (FE) formulation for the lateral torsional buckling (LTB) analyses of steel beams exteriorly bonded with orthotropic fiber-reinforced polymer (FRP) layers. The formulation considers shear deformations, partial material interaction, local and global warping deformations, and orthotropic FRP properties. The buckling responses of multispan FRP-bonded steel beams predicted by the present solutions are excellently validated against experiment and numerical solutions. As observed, the FRP strengthening is highly effective for the LTB resistance of steel beams. However, the LTB responses are strongly dependent on the orthotropic properties and strengthening lengths of FRP layers. The effects of shear deformations, span ratios, and loading conditions on the LTB responses are also quantified in the present study.

Keywords: lateral torsional buckling, finite element formulation, shear deformations, FRP strengthening, partial interaction, local and global warpings, orthotropic FRP layers, multispan beams

1 Introduction

Strengthening steel beams by using fiber-reinforced polymer (FRP) layers has been increasingly studied in order to upgrade their load capacities (e.g., [1–6]). The advantage of this

strengthening method is that the FRP layers are lightweight compared to bolted or welded steel plates, and FRP installation is relatively easy and quick. Most studies for the FRP strengthening method focused on using carbon fiber-reinforced polymer (CFRP) sheets that possess elasticity moduli higher than those of steel (e.g., [1–4]). Recently, glass FRP layers have been widely researched for the strengthening of steel structures because they are lower in cost than CFRP sheets, and they can be made by stacking GFRP laminae to form relatively thick layers [5–9]. When bonded to thin steel flanges, such thick FRP layers can considerably contribute to increase the system bending, shear, and twisting stiffnesses and thus they can strengthen the flanges to resist against buckling issues (e.g., [5–9]). In an experimental study conducted by El Damatty and Abushagur [5] for the LTB analysis of steel beams strengthened with FRP layers bonded to the top and bottom beam flanges, an increase of about 80% for the capacity of the FRP-strengthened steel beams was reported. The effectiveness of FRP strengthening was also observed in other studies (e.g., [6,7,9–16]).

FRP layers, however, have orthotropic behaviors because they are often created by stacking thin FRP laminae with different fiber stacking angles [9,17,18]. The flexural, shear, and torsional stiffnesses of FRP layers and FRP-bonded systems strongly depend on not only the longitudinal, transverse, and vertical dimensions of the FRP layers but also their number of laminae, fiber orientation angles, and stacking sequences [19]. Thus, the evaluation of the mechanical properties of such FRP-strengthened steel beams is relatively complicated. Also, an FRP layer bonded to a steel surface by a thin epoxy layer may generate a partial interaction between the steel and the FRP layer because the epoxy elasticity modulus is considerably lower than those of the steel and the FRP layer [6,14,15,19]. Besides, the effects of shear deformations on the torsional responses of such composite systems are considerable [20,21]. A theory neglecting the effects may incorrectly predict the torsional buckling responses of the FRP-strengthened steel beams (e.g., [20,21]). Finally, FRP layers are bonded to a part of the steel spans, and those create a beam having segments with different cross-sections (e.g., bare steel

* **Corresponding author: Phe Van Pham**, Faculty of Civil Engineering, University of Transport and Communications, #3 Cau Giay, Hanoi, Vietnam, e-mail: phe.phamvan@utc.edu.vn

Thi Doan-Tan: Faculty of Civil Engineering, Campus in Ho Chi Minh City, University of Transport and Communications, # 450-451 Le Van Viet, Ho Chi Minh City, Vietnam

Xuan-Huy Nguyen: Faculty of Construction Engineering, University of Transport and Communications, #3 Cau Giay, Hanoi, Vietnam

sections, FRP-bonded steel sections). The longitudinal lengths of the FRP layers may also influence the system buckling responses [22–24]. Such difficulties may challenge the design of an FRP strengthening solution for the steel members. In fact, the finite element (FE) analyses conducted in commercial software may be an option for the design. However, they usually involve complicated three-dimensional FE models and expensive computation costs. In such a case, the development of simpler solutions that can quickly and accurately predict the responses of the FRP-strengthened steel beams will bring more advantages to the design.

The LTB solutions have been widely developed for the analysis of multilayer beams (*e.g.*, [19,25–32]). Girhammar and Pan [25] developed a closed form solution for the prediction of the elastic LTB loads of two-layer beams. However, their study considered neither the partial interaction between layers nor the shear deformations. Xu and Wu [26] developed a shear deformable buckling theory for the analysis of two-layer members, in which the partial interaction between the two layers was considered. However, the theory was only applicable to rectangular cross-sections. Challamel and Girhammar [27] and Schnabl and Planinc [28] proposed non-shear deformable theories for the LTB analyses of vertically layered beams. Kabir and Seif [29] developed closed form solutions for the LTB loads of steel beams bonded with FRP sheets. Again, their models considered neither the partial interaction between steel and FRP layer nor the effect of shear deformations. Grognet *et al.* [30] developed a buckling solution for two-layer beams accounting for the shear deformations and partial interaction between layers. However, their models assumed isotropic materials to develop the buckling solution. Phe *et al.* [31] formulated an FE for the prediction of the LTB loads of a steel beam strengthened with a single FRP layer. However, the FRP was again treated as an isotropic material in their study. As a result, their model could not capture the orthotropic properties of FRP materials. Zaghian and Mohareb [32] developed a non-shear deformable finite shell element for the prediction of the elastic LTB of steel plates strengthened with isotropic FRP layers. However, the element was limited to the members with rectangular cross-sections. Recently, Phe [19] proposed a non-shear theory and developed a series of closed form solutions for the LTB loads of a group of the FRP-strengthened steel beams. Although his model captured the partial interaction between steel and FRP, shear deformations in steel beam were neglected and their solutions were restricted in application for single span steel beams strengthened with FRP layers. Thus, the solutions of Phe [19] were unable to predict the buckling loads of the FRP-strengthened continuous steel beams.

In this context, the present study fills in the shortcoming gap by developing an FE formulation for the prediction of the LTB analysis of single/continuous steel beams strengthened with orthotropic FRP layers. Specifically, the FE formulation can capture the effects of the shear deformations in both steel and FRP layers, which can remedy available solutions of previous studies [19,26–29,32]. Also, they considered the warping effects to be significant in beams with wide flange cross-sections, and they were not captured by previous studies [26,30,32]. The partial interactions between the steel beam and the FRP layers are included in the kinematic model of the present theory and were not considered in previous studies [25,29]. Besides, the present study accounts for the orthotropic properties of the FRP layers (*e.g.*, the number of orthotropic FRP laminae, fiber orientation angles, and stacking sequences) and was not considered by Phe *et al.* [31]. The shear deformable FE formulations of the present study are developed for both bare and FRP-strengthened steel elements. Such elements can be applied to the prediction of the LTB of single/continuous steel beams with various strengthening, boundary, and loading conditions, but these were not solved by the solutions of Phe [19]. Besides, the span interactions in continuous beams will be naturally captured by the present solutions, which were not considered in design guides of steel structures (*e.g.*, [33–35]), as also discussed in previous studies [36–38]. Based on the present solutions, the effects of the orthotropic FRP properties, the FRP strengthening lengths, and the loading conditions on the buckling responses of single/continuous steel beams strengthened with FRP layers will be quantified.

This article is presented in a sequence. A definition of the problem will be first stated in Section 2. An FE formulation will be then developed in Section 3, in which Section 3.1 proposes governing displacement fields of the composite system, Section 3.2 assumes the expressions of the buckling displacement fields in terms of the governing displacements, Sections 3.3 and 3.4 develop the buckling strains and stresses of the system, Sections 3.5 and 3.6 present the expressions of the total potential pre-buckling and buckling energies and their variations, and Section 3.7 presents the development of the FE formulation. The validation and result discussions of the buckling responses predicted by the present solution are presented in Section 4, and key conclusions are finally summarized in Section 5.

2 Statement of the problem

A wide flange steel element bonded with FRP layers 1 and 2 through Epoxy layers 1 and 2 and subjected to distributed and point loads $q_y(z_q, y_q)$, $P_y(z_p, y_p)$ is considered (Figure 1a and b). The cross-sectional dimensions of the wide flange

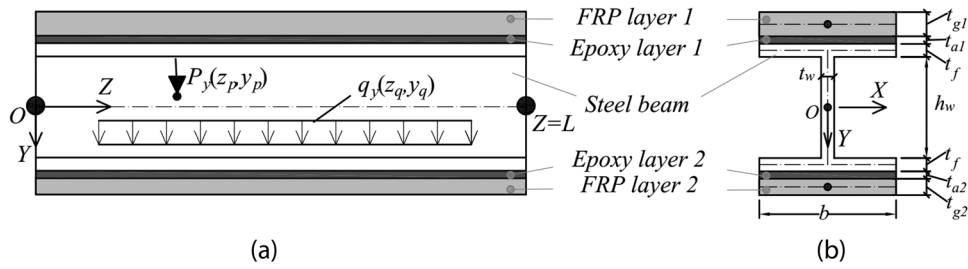


Figure 1: Profile (a) and cross-section (b) of the present FE.

section are $h_w t_w$, b , and t_f . The thicknesses of FRP layers 1 and 2 are t_{g1} and t_{g2} , respectively. While those of Epoxy layer 1 and Epoxy layer 2 are t_{a1} and t_{a2} , respectively. The mechanical properties of steel, epoxy, and orthotropic FRP materials are later defined in the formulation. A new FE formulation for the prediction of the elastic lateral torsional (LT) buckling of such a composite system is developed in the present study.

3 FE formulation

3.1 Governing displacement fields and kinematic model assumptions

When the system is switched from the onset of buckling (*i.e.*, a static equilibrium state) into the buckled mode (*i.e.*, a buckling equilibrium state), as depicted in Figure 2, eight governing displacements $U_b(z)$, $\theta_{yb}(z)$, $U_{1b}(z)$, $\theta_{y1b}(z)$, $U_{2b}(z)$, $\theta_{y2b}(z)$, $\theta_{zb}(z)$, and $\psi_b(z)$ are proposed to describe the buckling mode (Figure 3a–c), in which $U_b(z)$ is the lateral displacement at the centroid of the steel cross-section, $\theta_{yb}(z)$ is the lateral bending slope of the steel beam, $U_{1b}(z)$ is the lateral displacement at the centroid of FRP layer 1, $\theta_{y1b}(z)$ is

the lateral bending slope of FRP layer 1, $U_{2b}(z)$ is the lateral displacement at the centroid of FRP layer 2, $\theta_{y2b}(z)$ is the lateral bending slope of FRP layer 2, $\theta_{zb}(z)$ is the twisting angle of all materials, and $\psi_b(z)$ is the global warping deformation of the steel section.

In the present theory, the following four kinematic assumptions are made: (i) shear deformations caused by transverse bending, lateral bending, and global warping are captured, (ii) local warping deformations of solid rectangular cross-sectional parts (*e.g.*, the steel flanges, the steel webs, and the FRP layers) are proportional to the slope of the twisting angle $\theta'_{zb}(z)$ (Figure 2c), and (iii) the partial interaction occurs at the epoxy layer, where the epoxy displacements are linearly interpolated from the steel and the FRP layer displacements.

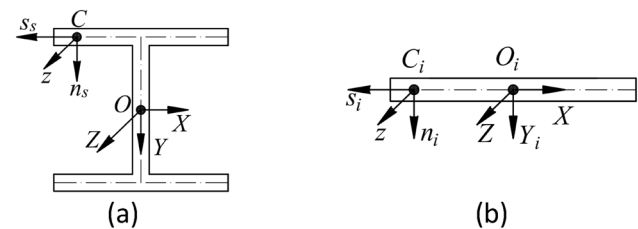


Figure 3: Coordinate systems in (a) the steel cross-section and (b) epoxy and FRP layers.

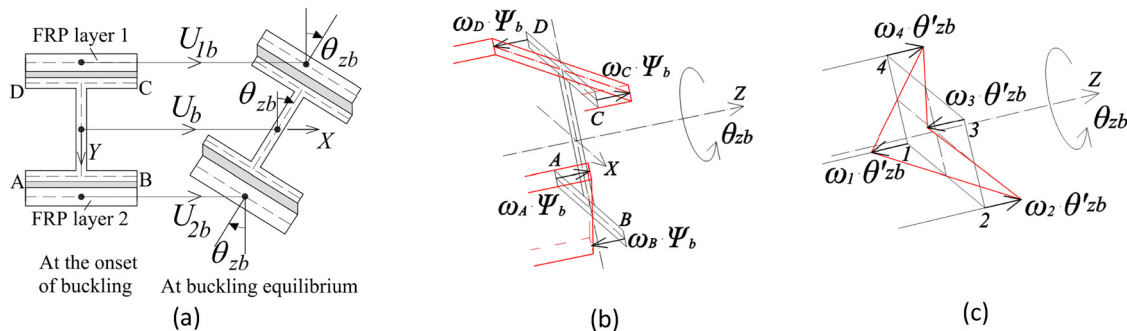


Figure 2: Governing displacement fields in the steel beams and FRP layers in the lateral-torsional buckling equilibrium state: (a) a part of cross-section view, (b) global warping deformations in the steel section, and (c) local warping deformations in the solid rectangular cross-sectional parts.

3.2 Expression of buckling displacement fields

Five global coordinate systems are selected for the five materials, as presented in Figure 3, in which $OXYZ$ is that of the steel cross-section and O_iXY_iZ with $i = g1$ is that of FRP layer 1, with $i = g2$ is that of FRP layer 2, with $i = a1$ is that of Epoxy layer 1, and with $i = a2$ is that of Epoxy layer 2. Origins O and O_i are the centroids of the cross-sections, X is the lateral axis, Y_i are the transverse axes, and Z is the axial axis. Also, local coordinate systems $C_s s_n z$ and $C_i s_i n_i z$ are assigned to the sectional contour (Figure 3), where origins C and C_i lie on the sectional contours, s_s is the curvilinear contour coordinate measured from the origins, n_s is the normal-to-tangent axis of the contour measured from the contour, and z is the longitudinal axis.

Buckling displacement fields at a point with coordinates (s_s, n_s, z) in the steel are denoted as u_s , v_s , and w_s (Figure 3a). Based on a shear deformable theory [20,39,40], they can be expressed in terms of the governing displacements as

$$\begin{aligned} w_s(s_s, n_s, z) &= -n_s \sin \alpha(s_s) U_b'(z) - x(s_s) \theta_{yb}(z) \\ &\quad + n_s q(s_s) \theta_{zb}'(z) - \omega(s_s) \psi_b(z); \\ u_s(s_s, n_s, z) &= \cos \alpha(s_s) U_b(z) + [r(s_s) + n_s] \theta_{zb}(z); \\ v_s(s_s, n_s, z) &= \sin \alpha(s_s) U_b(z) - q(s_s) \theta_{zb}(z). \end{aligned} \quad (1)$$

Here, $q(s_s) = x(s_s) \cos \alpha(s_s) + y(s_s) \sin \alpha(s_s)$ and $r(s_s) = x(s_s) \sin \alpha(s_s) - y(s_s) \cos \alpha(s_s)$. $\alpha(s_s)$ is an angle between the positive directions of the s_s axis and X -axis (Figure 4a) and it is taken positive in the clockwise direction from the X -axis. $\omega(s_s) = \int_0^{s_s} r(s_s) ds_s$ is the sectorial coordinate of the point being considered. The buckling displacement fields at a point along the coordinates (s_{g1}, n_{g1}, z) in FRP layer 1

are denoted as u_{g1} , v_{g1} , w_{g1} and they can be assumed as [20,39,40]

$$\begin{aligned} w_{g1}(s_{g1}, n_{g1}, z) &= -x(s_{g1}) \theta_{y1b}(z) + n_{g1} x(s_{g1}) \theta_{zb}'(z); \\ u_{g1}(s_{g1}, n_{g1}, z) &= U_{1b}(z) + n_{g1} \theta_{zb}(z); \\ v_{g1}(s_{g1}, n_{g1}, z) &= -x(s_{g1}) \theta_{zb}(z). \end{aligned} \quad (2)$$

Also, the displacement fields at a point with coordinates (s_{g2}, n_{g2}, z) in FRP layer 2 are u_{g2} , v_{g2} , w_{g2} and can be expressed as [20,39,40]

$$\begin{aligned} w_{g2}(s_{g2}, n_{g2}, z) &= -x(s_{g2}) \theta_{y2b}(z) + n_{g2} x(s_{g2}) \theta_{zb}'(z); \\ u_{g2}(s_{g2}, n_{g2}, z) &= U_{2b}(z) + n_{g2} \theta_{zb}(z); \\ v_{g2}(s_{g2}, n_{g2}, z) &= -x(s_{g2}) \theta_{zb}(z). \end{aligned} \quad (3)$$

The buckling displacement fields at a point along coordinates (s_{a1}, n_{a1}, z) in Epoxy layer 1 are denoted as u_{a1} , v_{a1} , w_{a1} . Based on Assumption (iii), they are linearly interpolated from the displacements at the uppermost steel fiber (i.e., $n_s = t_f/2$) and those at the bottom of FRP layer 1 (i.e., $n_{g1} = -t_{g1}/2$), i.e.,

$$\begin{aligned} w_{a1}(s_{a1}, n_{a1}, z) &= \left(\frac{1}{2} - \frac{n_{a1}}{t_{a1}} \right) w_s \left(s_s, \frac{t_f}{2}, z \right) \\ &\quad + \left(\frac{1}{2} + \frac{n_{a1}}{t_{a1}} \right) w_{g1} \left(s_{g1}, -\frac{t_{g1}}{2}, z \right); \\ u_{a1}(s_{a1}, n_{a1}, z) &= \left(\frac{1}{2} - \frac{n_{a1}}{t_{a1}} \right) u_s \left(s_s, \frac{t_f}{2}, z \right) \\ &\quad + \left(\frac{1}{2} + \frac{n_{a1}}{t_{a1}} \right) u_{g1} \left(s_{g1}, -\frac{t_{g1}}{2}, z \right); \\ v_{a1}(s_{a1}, n_{a1}, z) &= \left(\frac{1}{2} - \frac{n_{a1}}{t_{a1}} \right) v_s \left(s_s, \frac{t_f}{2}, z \right) \\ &\quad + \left(\frac{1}{2} + \frac{n_{a1}}{t_{a1}} \right) v_{g1} \left(s_{g1}, -\frac{t_{g1}}{2}, z \right). \end{aligned} \quad (4)$$

From Eqs. (1) and (2), by setting $n_s = t_f/2$, $n_{g1} = -t_{g1}/2$ and by substituting into Eq. (4), we have

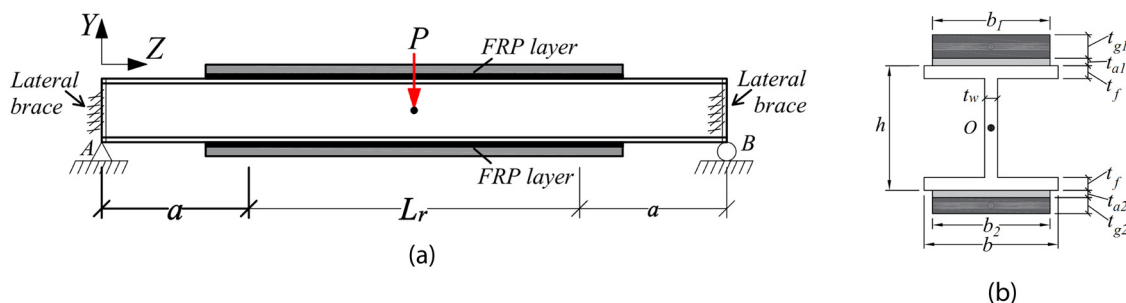


Figure 4: Profile (a) and cross-section (b) of the FRP layer-bonded steel beam in Example 1.

$$\begin{aligned}
w_{a1}(s_{a1}, n_{a1}, z) &= -\left(\frac{1}{2} - \frac{n_{a1}}{t_{a1}}\right)x(s)\theta_{yb}(z) \\
&\quad - \left(\frac{1}{2} + \frac{n_{a1}}{t_{a1}}\right)x(s)\theta_{y1b}(z) \\
&\quad + \left[\frac{(t_f - t_{g1})}{4} - \frac{(t_f + t_{g1})n_{a1}}{2t_{a1}}\right]x(s)\theta'_{zb} \\
&\quad \times (z) - \frac{h_b}{2}\left(\frac{1}{2} - \frac{n_{a1}}{t_{a1}}\right)x(s)\psi_b(z); \quad (5)
\end{aligned}$$

$$\begin{aligned}
u_{a1}(s_{a1}, n_{a1}, z) &= \left(\frac{1}{2} - \frac{n_{a1}}{t_{a1}}\right)U_b(z) + \left(\frac{1}{2} + \frac{n_{a1}}{t_{a1}}\right)U_{1b}(z) \\
&\quad + \left[\frac{h - t_{g1}}{4} - \frac{(h + t_{g1})n_{a1}}{2t_{a1}}\right]\theta_{zb}(z); \\
v_{a1}(s_{a1}, n_{a1}, z) &= -x(s)\theta_{zb}(z).
\end{aligned}$$

For Epoxy layer 2, the buckling displacement fields at a point along coordinates (s_{a2}, n_{a2}, z) are denoted as u_{a2}, v_{a2}, w_{a2} . They are linearly interpolated from the displacements at the lowermost steel fiber and those at the top of the FRP layer 2, i.e.,

$$\begin{aligned}
w_{a2}(s_{a2}, n_{a2}, z) &= \left(\frac{1}{2} + \frac{n_{a2}}{t_{a2}}\right)w_s\left(s_s, -\frac{t_f}{2}, z\right) \\
&\quad + \left(\frac{1}{2} - \frac{n_{a2}}{t_{a2}}\right)w_{g2}\left(s_{g2}, \frac{t_{g2}}{2}, z\right); \\
u_{a2}(s_{a2}, n_{a2}, z) &= \left(\frac{1}{2} + \frac{n_{a2}}{t_{a2}}\right)u_s\left(s_s, -\frac{t_f}{2}, z\right) \\
&\quad + \left(\frac{1}{2} - \frac{n_{a2}}{t_{a2}}\right)u_{g2}\left(s_{g2}, \frac{t_{g2}}{2}, z\right); \quad (6) \\
v_{a2}(s_{a2}, n_{a2}, z) &= \left(\frac{1}{2} + \frac{n_{a2}}{t_{a2}}\right)v_s\left(s_s, -\frac{t_f}{2}, z\right) \\
&\quad + \left(\frac{1}{2} - \frac{n_{a2}}{t_{a2}}\right)v_{g2}\left(s_{g2}, \frac{t_{g2}}{2}, z\right).
\end{aligned}$$

From Eqs. (1) and (2), by setting $n_s = -t_f/2$, $n_{g2} = t_{g2}/2$ and substituting into Eq. (6), we have

$$\begin{aligned}
w_{a2}(s_{a2}, n_{a2}, z) &= -\left(\frac{1}{2} + \frac{n_{a2}}{t_{a2}}\right)x(s_{a2})\theta_{yb}(z) \\
&\quad - \left(\frac{1}{2} - \frac{n_{a2}}{t_{a2}}\right)x(s_{a2})\theta_{y2b}(z) \\
&\quad - \left[\frac{(t_f - t_{g2})}{4} + \frac{(t_f + t_{g2})n_{a2}}{2t_{a2}}\right]x(s_{a2})\theta'_{zb} \\
&\quad \times (z) + \frac{h_b}{2}\left(\frac{1}{2} + \frac{n_{a2}}{t_{a2}}\right)x(s_{a2})\psi_b(z); \quad (7) \\
u_{a2}(s_{a2}, n_{a2}, z) &= \left(\frac{1}{2} + \frac{n_{a2}}{t_{a2}}\right)U_b(z) + \left(\frac{1}{2} - \frac{n_{a2}}{t_{a2}}\right)U_{2b}(z) \\
&\quad - \left[\frac{(h - t_{g2})}{4} + \frac{(h + t_{g2})n_{a2}}{2t_{a2}}\right]\theta_{zb}(z); \\
v_{a2}(s_{a2}, n_{a2}, z) &= -x(s_{a2})\theta_{zb}(z).
\end{aligned}$$

3.3 Expression of buckling strain fields

The buckling normal and shear strains in the steel member and the FRP layers are often obtained as

$$\begin{aligned}
\varepsilon_i &= \frac{\partial w_i}{\partial z} + \frac{1}{2}\left[\left(\frac{\partial v_i}{\partial z}\right)^2 + \left(\frac{\partial u_i}{\partial z}\right)^2\right], \quad (8) \\
\gamma_{i,sz} &= \frac{\partial u_i}{\partial z} + \frac{\partial w_i}{\partial s_i} + \frac{\partial u_i}{\partial z} \frac{\partial u_i}{\partial s_i} + \frac{\partial w_i}{\partial s_i} \frac{\partial w_i}{\partial z} + \frac{\partial v_i}{\partial s_i} \frac{\partial v_i}{\partial z},
\end{aligned}$$

where $i = s$ denotes the steel member, $i = g1$ denotes FRP layer 1, and $i = g2$ denotes FRP layer 2. The normal and shear strains in the steel beam can be obtained by substituting Eq. (1) into Eq. (8) to yield the following expressions:

$$\begin{aligned}
\varepsilon_s &= -n_s \sin \alpha(s_s)U_b''(z) - x(s_s)\theta'_{yb}(z) + n_s q(s_s)\theta''_{zb}(z) \\
&\quad - \omega(s_s)\psi_b'(z) + \frac{1}{2}U_b'^2(z) + [n_s \cos \alpha(s_s) \\
&\quad - y(s_s)]U_b'(z)\theta'_{zb}(z) + \frac{1}{2}q^2(s_s)\theta_{zb}^2(z) \\
&\quad + \frac{1}{2}[r(s_s) + n_s]^2\theta_{zb}^2(z), \quad (9)
\end{aligned}$$

$$\begin{aligned}
\gamma_{s,sz} &= +\cos \alpha(s_s)U_b'(z) - \cos \alpha(s_s)\theta_{yb}(z) \\
&\quad + \{r(s_s) + 2n_1 q'(s_s)\}\theta'_{zb}(z) - \omega'(s_s)\psi_b(z) \\
&\quad - q'(s_s) \sin \alpha(s_s)U_b'(z)\theta_{zb}(z) \\
&\quad - n_s^2 q'(s_s) \sin \alpha(s_s)U_b''(z)\theta'_{zb}(z) \\
&\quad + n_1 \omega'(s_s) \sin \alpha(s_s)U_b''(z)\psi_b(z) \\
&\quad + x(s_s) \cos \alpha(s_s)\theta_{yb}(z)\theta'_{yb}(z) \\
&\quad - n_s q(s_s) \cos \alpha(s_s)\theta_{yb}(z)\theta''_{zb}(z) \\
&\quad + \omega(s_s) \cos \alpha(s_s)\theta_{yb}(z)\psi_b'(z) \\
&\quad + q(s_s)q'(s_s)\theta_{zb}(z)\theta'_{zb}(z) - x(s_s)n_s q'(s_s)\theta'_{yb}(z)\theta'_{zb}(z) \\
&\quad + x(s_s)\omega'(s_s)\theta'_{yb}(z)\psi_b(z) + n_s^2 q(s_s)q'(s_s)\theta'_{zb}(z)\theta''_{zb}(z) \\
&\quad - \omega(s_s)n_s q'(s_s)\theta'_{zb}(z)\psi_b'(z) \\
&\quad - \omega'(s_s)n_s q(s_s)\theta''_{zb}(z)\psi_b(z) + \omega(s_s)\omega'(s_s)\psi_b'(z)\psi_b(z). \quad (10)
\end{aligned}$$

The normal and shear strains in FRP layer 1 can be obtained by substituting Eq. (2) into Eq. (8), i.e.,

$$\varepsilon_{g1} = \varepsilon_{g1,zz}^* + n_{g1}\kappa_{g1,zz}^*, \quad \gamma_{g1,sz} = \gamma_{g1,sz}^* + n_{g1}\kappa_{g1,sz}^*, \quad (11)$$

where

$$\begin{aligned}
\varepsilon_{g1,zz}^* &= -x(s_{g1})\theta'_{y1b}(z) + \frac{1}{2}U_{1b}^2(z) + \frac{1}{2}x^2(s_{g1})\theta_{zb}^2(z); \\
\kappa_{g1,zz}^* &= x(s_{g1})\theta'_{zb}(z) + U'_{1b}(z)\theta'_{zb}(z); \\
\gamma_{g1,sz}^* &= U'_{1b}(z) - \theta_{y1b}(z) + x(s_{g1})\theta'_{y1b}(z)\theta_{y1b}(z) \\
&\quad + x(s_{g1})\theta_{zb}(z)\theta'_{zb}(z); \quad (12) \\
\kappa_{g1,sz}^* &= +2\theta'_{zb}(z) - x(s_{g1})\theta'_{y1b}(z)\theta'_{zb}(z) \\
&\quad - x(s_{g1})\theta_{y1b}(z)\theta'_{zb}(z).
\end{aligned}$$

Also, the normal and shear strains in FRP layer 2 can be obtained by substituting Eq. (3) into Eq. (8), i.e.,

$$\varepsilon_{g2}^* = \varepsilon_{g2,zz}^* + n_{g2}\kappa_{g2,zz}^*, \quad \gamma_{g2,sz} = \gamma_{g2,sz}^* + n_{g2}\kappa_{g2,sz}^*, \quad (13)$$

where

$$\begin{aligned} \varepsilon_{g2,zz}^* &= -x(s_{g2})\theta'_{yb}(z) + \frac{1}{2}U_{2b}'^2(z) + \frac{1}{2}x^2(s_{g2})\theta_{2b}'^2(z), \\ \kappa_{g2,zz}^* &= x(s_{g2})\theta''_{zb}(z) + U_{2b}'(z)\theta'_{zb}(z), \\ \gamma_{g2,sz}^* &= U_{2b}'(z) - \theta_{yb}(z) + x(s_{g2})\theta'_{yb}(z)\theta_{yb}(z) \\ &\quad + x(s_{g2})\theta_{zb}(z)\theta'_{zb}(z), \\ \kappa_{g2,sz}^* &= +2\theta'_{zb}(z) - x(s_{g2})\theta'_{yb}(z)\theta'_{zb}(z) \\ &\quad - x(s_{g2})\theta_{yb}(z)\theta''_{zb}(z). \end{aligned} \quad (14)$$

The deformations of epoxy layers are assumed to be mostly contributed by shear strains. The following three shear strains in the epoxy layers are obtained as

$$\begin{aligned} \gamma_{i,zn} &= \frac{\partial v_i}{\partial z} + \frac{\partial w_i}{\partial n_i} + \frac{\partial v_i}{\partial z} \frac{\partial v_i}{\partial n_i} + \frac{\partial w_i}{\partial z} \frac{\partial w_i}{\partial n_i} + \frac{\partial u_i}{\partial z} \frac{\partial u_i}{\partial n_i}; \\ \gamma_{i,sn} &= \frac{\partial v_i}{\partial s_i} + \frac{\partial u_i}{\partial n_i} + \frac{\partial v_i}{\partial s_i} \frac{\partial v_i}{\partial n_i} + \frac{\partial u_i}{\partial s_i} \frac{\partial u_i}{\partial n_i} + \frac{\partial w_i}{\partial s_i} \frac{\partial w_i}{\partial n_i}; \\ \gamma_{i,sz} &= \frac{\partial u_i}{\partial z} + \frac{\partial w_i}{\partial s_i} + \frac{\partial u_i}{\partial z} \frac{\partial u_i}{\partial s_i} + \frac{\partial w_i}{\partial z} \frac{\partial w_i}{\partial s_i} + \frac{\partial v_i}{\partial z} \frac{\partial v_i}{\partial s_i}; \end{aligned} \quad (15)$$

in which subscript $i = a1$ denotes Epoxy layer 1 and $i = a2$ denotes Epoxy layer 2. The shear strains in Epoxy layer 1 can be expressed in terms of governing displacement fields by substituting Eq. (5) into Eq. (15) and neglecting nonlinear terms, i.e.,

$$\begin{aligned} \gamma_{a1,zn} &= \frac{1}{t_{a1}}x(s_{a1})\theta_{yb}(z) - \frac{1}{t_{a1}}x(s_{a1})\theta_{y1b}(z) \\ &\quad - \left[\frac{t_f + t_{g1}}{2t_{a1}} + 1 \right] x(s_{a1})\theta'_{zb}(z) + \frac{h_b}{2t_{a1}}x(s_{a1})\psi_b(z); \\ \gamma_{a1,sn} &= -\frac{1}{t_{a1}}U_b(z) + \frac{1}{t_{a1}}U_{1b}(z) - \frac{h + 2t_{a1} + t_{g1}}{2t_{a1}}\theta_{zb}(z); \\ \gamma_{a1,sz} &= \left(\frac{1}{2} - \frac{n_{a1}}{t_{a1}} \right) U_b'(z) - \left(\frac{1}{2} - \frac{n_{a1}}{t_{a1}} \right) \theta_{yb}(z) \\ &\quad + \left(\frac{1}{2} + \frac{n_{a1}}{t_{a1}} \right) U_{1b}'(z) - \left(\frac{1}{2} + \frac{n_{a1}}{t_{a1}} \right) \theta_{y1b}(z) \\ &\quad + \left[\frac{h + t_f - 2t_{g1}}{4} - \frac{(h + t_f + 2t_{g1})n_{a1}}{2t_{a1}} \right] \theta'_{zb}(z) \\ &\quad - \frac{h_b}{2} \left(\frac{1}{2} - \frac{n_{a1}}{t_{a1}} \right) \psi_b(z). \end{aligned} \quad (16)$$

Also, the shear strains in Epoxy layer 2 can be expressed in terms of governing displacement fields by substituting Eq. (7) into Eq. (15) and neglecting nonlinear terms, i.e.,

$$\begin{aligned} \gamma_{a2,zn} &= -\frac{1}{t_{a2}}x(s_{a2})\theta_{yb} + \frac{1}{t_{a2}}x(s_{a2})\theta_{y2b}(z) \\ &\quad - \left[\frac{(t_f + t_{g2})}{2t_{a2}} + 1 \right] x(s_{a2})\theta'_{zb}(z) \\ &\quad + \frac{h_b}{2t_{a2}}x(s_{a2})\psi_b(z); \\ \gamma_{a2,sn} &= \frac{1}{t_{a2}}U_b(z) - \frac{1}{t_{a2}}U_{2b}(z) - \left[\frac{h + t_{g2}}{2t_{a2}} + 1 \right] \theta_{zb}(z); \\ \gamma_{a2,sz} &= \left(\frac{1}{2} + \frac{n_{a2}}{t_{a2}} \right) U_b'(z) - \left(\frac{1}{2} + \frac{n_{a2}}{t_{a2}} \right) \theta_{yb}(z) \\ &\quad + \left(\frac{1}{2} - \frac{n_{a2}}{t_{a2}} \right) U_{2b}'(z) - \left(\frac{1}{2} - \frac{n_{a2}}{t_{a2}} \right) \theta_{y2b}(z) \\ &\quad - \left[\frac{h + t_f - 2t_{g2}}{4} + \frac{(h + t_f + 2t_{g2})n_{a2}}{2t_{a2}} \right] \theta'_{zb}(z) \\ &\quad + \frac{h_b}{2} \left(\frac{1}{2} + \frac{n_{a2}}{t_{a2}} \right) \psi_b(z). \end{aligned} \quad (17)$$

3.4 Expression of buckling stresses and stress resultants

Steel has an elastic modulus E_s , a shear modulus G_s , and a Poisson's ratio μ . The steel stress-strain relations are thus expressed as

$$\sigma_s = E_s \varepsilon_s, \quad \tau_{s,sz} = G_s \gamma_{s,sz}. \quad (18)$$

FRP layers are assumed to be stacked by n FRP laminae [19]. The FRP laminae are symmetrically balanced about the middle height of the layer. FRP lamina k (where $k = 1, 2, \dots, n$) has an axial elasticity modulus $E_{k,z}$, a lateral elasticity modulus $E_{k,s}$, a shear modulus $G_{k,sz}$, and Poisson's ratio $\nu_{k,zs}$, $\nu_{k,sz}$. Based on the theories of composite structures [19,40–43], the FRP strain-stress resultant relations can be obtained as

$$\begin{aligned} N_{gi,zz}^* &= \bar{A}_{gi,11} \varepsilon_{gi,zz}^*, & N_{gi,xz}^* &= \bar{A}_{gi,66} \gamma_{gi,xz}^*, \\ M_{gi,zz}^* &= \bar{D}_{gi,11} \kappa_{gi,zz}^*, & M_{gi,xz}^* &= \bar{D}_{gi,66} \kappa_{gi,xz}^*, \end{aligned} \quad (19)$$

where $N_{gi,zz}^*$, $N_{gi,xz}^*$, $M_{gi,zz}^*$, and $M_{gi,xz}^*$ ($i = 1$ or 2) are the stress resultants in the FRP layer i . Plate stiffnesses $\bar{A}_{gi,11}$, $\bar{A}_{gi,66}$, $\bar{D}_{gi,11}$, $\bar{D}_{gi,66}$ in Eq. (19) are evaluated and presented in Appendix 1. The shear stress-strain relationships in Epoxy layers i ($i = 1, 2$) are assumed as

$$\tau_{ai,zn} = G_{ai} \gamma_{ai,zn}, \quad \tau_{ai,sn} = G_{ai} \gamma_{ai,sn}, \quad \tau_{ai,sz} = G_{ai} \gamma_{ai,sz}, \quad (20)$$

where G_{ai} is the shear modulus of the epoxy material.

3.5 Pre-buckling analysis

A pre-buckling analysis is necessary to obtain pre-buckling internal forces that contribute to the geometric buckling stiffnesses of the system. The total in-plane pre-buckling potential energy π_p of the system is contributed by a pre-buckling internal strain energy of π_{pU} and a pre-buckling load potential energy of π_{pV} . When the system is in a static equilibrium state, the first variation of the energy $\delta\pi_p$ vanishes [44], i.e.,

$$\delta\pi_p = \delta(\pi_{pU} + \pi_{pV}) = 0, \quad (21)$$

in which the pre-buckling internal strain energy π_{pU} can be obtained by the following expression:

$$\begin{aligned} \pi_{pU} = & \frac{1}{2} \left[\int_0^L \int_{A_s} E_s \varepsilon_{ps}^2 dA_s dz + \int_0^L \int_{A_s} G_s \gamma_{ps,sz}^2 dA_s dz \right. \\ & + \int_0^L \int_0^b \bar{A}_{g1,11} \varepsilon_{pg1,zz}^2 dx dz + \int_0^L \int_0^b \bar{D}_{g1,11} \kappa_{pg1,zz}^2 dx dz \\ & + \int_0^L \int_{A_{a1}} G_{a1} \gamma_{pa1,nz}^2 dA_{a1} dz + \int_0^L \int_0^{b_2} \bar{A}_{g2,11} \varepsilon_{pg2,zz}^2 dx dz \\ & \left. + \int_0^L \int_0^{b_2} \bar{D}_{g2,11} \kappa_{pg2,zz}^2 dx dz + \int_0^L \int_{A_{a2}} G_{a2} \gamma_{pa2,nz}^2 dA_{a2} dz \right], \end{aligned} \quad (22)$$

where the pre-buckling strains in Eq. (22) can be obtained as [41]

$$\begin{aligned} \varepsilon_{ps} &= W_p'(z) + n_s \cos \alpha(s_s) V_p''(z) - y(s_s) \theta_{xp}'(z), \\ \gamma_{ps,sz} &= \sin \alpha(s_1) \{ V_p'(z) - \theta_{xp}(z) \}, \\ \varepsilon_{pg1,zz}^* &= W_p'(z), \\ \kappa_{pg1,zz}^* &= V_p''(z), \\ \varepsilon_{pg2,zz}^{*pre} &= W_{2p}'(z), \\ \kappa_{pg2,zz}^{*pre} &= V_p''(z), \\ \gamma_{pa1,nz} &= -\frac{1}{t_{a1}} W_p(z) + \frac{1}{t_{a1}} W_{1p}(z) \\ &\quad - \frac{(2t_{a1} + t_f + t_{g1})}{2t_{a1}} V_p'(z) - \frac{h_b}{2t_{a1}} \theta_{xp}(z), \\ \gamma_{pa2,nz} &= \frac{1}{t_{a2}} W_p(z) - \frac{1}{t_{a2}} W_{2p}(z) \\ &\quad - \frac{(2t_{a2} + t_f + t_{g2})}{2t_{a2}} V_p'(z) - \frac{h_b}{2t_{a2}} \theta_{xp}(z). \end{aligned} \quad (23)$$

Here, $W_p(z)$, $W_{1p}(z)$, $W_{2p}(z)$ are, respectively, the longitudinal governing displacement field of the cross-sectional centroid of the steel beam, that of the cross-sectional centroid of the FRP layer 1, and that of the cross-sectional centroid of the FRP layer 2. Also, $V_p(z)$ is the vertical

governing displacement field of the composite section, while $\theta_{xp}(z)$ is the slope of the vertical displacement field of the composite section [41]. In Eq. (21), π_{pV} is the load potential energy caused by in-plane pre-buckling loads and has been defined in the study of Thanh and Phe [41]. From Eq. (23), by substituting into Eq. (22), an expression of π_{pU} in terms of the pre-buckling governing displacement fields can be obtained. Based on expressions of π_{pU} , by substituting into Eq. (21) and taking the first variation of the total potential energy π_p , a system of equilibrium equations and corresponding boundary conditions can be obtained. By solving such a problem, solutions of the in-plane governing displacements and the pre-buckling internal forces of the system can be obtained. This procedure was solved by Thanh and Phe [41]. The present study takes the pre-buckling stress resultants from that solution for the development of the present buckling FE formulation. The in-plane pre-buckling strains of the system can be expressed in terms of the in-plane pre-buckling stress resultant as follows:

$$\begin{aligned} \varepsilon_{ps} &= \frac{N_p(z)}{E_s A_s} + n_s \cos \alpha(s_s) \frac{M_{ss}}{I_{ss}} - y(s_s) \frac{M_{xs}}{I_{xx}}, \\ \gamma_{ps,sz} &= \sin \alpha(s_1) \frac{Q_p}{A_w}, \\ \varepsilon_{pg1,zz} &= \frac{N_{1p}}{b A_{g1,11}}, \quad \kappa_{pg1,zz} = \frac{M_{ss}}{b D_{g1,11}}, \\ \varepsilon_{pg2,zz} &= \frac{N_{2p}}{b A_{g2,11}}, \quad \kappa_{pg2,zz} = \frac{M_{ss}}{b D_{g2,11}}, \end{aligned} \quad (24)$$

where $N_p(z)$, $N_{1p}(z)$, $N_{2p}(z)$, $Q_p(z)$, $M_{ss}(z)$, $M_{xs}(z)$ are the stress resultants associated with the governing displacement fields $W_p(z)$, $W_{1p}(z)$, $W_{2p}(z)$, $V_p(z)$, $V_p'(z)$, $\theta_{xp}(z)$. The mechanical properties of the steel are $I_{ss} = 2bt_f^3/12$, $I_{xx} = bt_f h_w^2/2 + t_w h_w^3/12$, $A_s = 2bt_f + h_w t_w$, $A_w = h_w t_w$, while $A_{gi,11}$, $D_{gi,11}$ of the FRP layers are defined in Appendix 1.

3.6 Buckling analysis

The total buckling potential energy of the system and its variational computations are developed in this section. When the system is in the buckling equilibrium state, the variation of the second variation of the total buckling potential energy π of the system should vanish [44], i.e.,

$$\delta \left[\frac{1}{2} \delta^2 \pi \right] = \delta \left[\frac{1}{2} (\delta^2 U + \delta^2 V) \right] = 0. \quad (25)$$

Here, U is the total buckling strain energy and V is the total load potential loss. The strain energy U is obtained as

$$\begin{aligned}
U = & \int_0^L \int_{A_s} \varepsilon_s \sigma_s dA_s dz + \int_0^L \int_{A_s} \gamma_{s,sz} \tau_{s,sz} dA_s dz + \int_0^L \int_0^{b_1} \varepsilon_{g1,zz}^* N_{g1,zz}^* dA_{g1} dz + \int_0^L \int_0^{b_1} \kappa_{g1,zz}^* M_{g1,zz}^* dA_{g1} dz + \int_0^L \int_0^{b_1} \gamma_{g1,sz}^* N_{g1,sz}^* dA_{g1} dz \\
& + \int_0^L \int_0^{b_1} \kappa_{g1,sz}^* M_{g1,sz}^* dA_{g1} dz + \int_0^L \int_{A_{a1}} (\gamma_{a1,zn} \tau_{a1,zn} + \gamma_{a1,sn} \tau_{a1,sn} + \gamma_{a1,sz} \tau_{a1,sz}) dA_{a2} dz + \int_0^L \int_0^{b_2} \varepsilon_{g2,zz}^* N_{g2,zz}^* dA_{g2} dz \\
& + \int_0^L \int_0^{b_2} \kappa_{g2,zz}^* M_{g2,zz}^* dA_{g2} dz + \int_0^L \int_0^{b_2} \gamma_{g2,sz}^* N_{g2,sz}^* dA_{g2} dz + \int_0^L \int_0^{b_2} \kappa_{g2,sz}^* M_{g2,sz}^* dA_{g2} dz \\
& + \int_0^L \int_{A_{a2}} (\gamma_{a2,zn} \tau_{a2,zn} + \gamma_{a2,sn} \tau_{a2,sn} + \gamma_{a2,sz} \tau_{a2,sz}) dA_{a2} dz.
\end{aligned} \tag{26}$$

From Eq. (26), by substituting stresses in Section 3.4 and taking the second variation with respect to the strains, we have

$$\begin{aligned}
\frac{1}{2} \delta^2 U = & \frac{1}{2} \left[\int_0^L \int_{A_s} E_s [(\delta \varepsilon_s^{bL})^2 + \varepsilon_{ps} \delta^2 \varepsilon_s^{bN}] dA_s dz + \int_0^L \int_{A_s} G_s [(\delta \gamma_s^{bL})^2 + \gamma_{ps} \delta^2 \gamma_s^{bN}] dA_s dz \right. \\
& + \int_0^L \int_0^b \bar{A}_{g1,11} [(\delta \varepsilon_{g1,zz}^{bL})^2 + \varepsilon_{pg1,zz} \delta^2 \varepsilon_{g1,zz}^{bN}] dx dz + \int_0^L \int_0^b \bar{D}_{g1,11} [(\delta \kappa_{g1,zz}^{bL})^2 + \kappa_{pg1,zz} \delta^2 \kappa_{g1,zz}^{bN}] dx dz + \int_0^L \int_0^b \bar{A}_{g1,66} (\delta \gamma_{g1,sz}^{bL})^2 dx dz \\
& + \int_0^L \int_0^b \bar{D}_{g1,66} (\delta \kappa_{g1,sz}^{bL})^2 dx dz + \int_0^L \int_{A_{a1}} G_{a1} (\delta \gamma_{a1,zn}^{bL})^2 dA_{a1} dz + \int_0^L \int_{A_{a1}} G_{a1} (\delta \gamma_{a1,sn}^{bL})^2 dA_{a1} dz + \int_0^L \int_{A_{a1}} G_{a1} (\delta \gamma_{a1,sz}^{bL})^2 dA_{a1} dz \\
& + \int_0^L \int_0^b \bar{A}_{g2,11} [(\delta \varepsilon_{g2,zz}^{bL})^2 + \varepsilon_{pg2,zz} \delta^2 \varepsilon_{g2,zz}^{bN}] dx dz + \int_0^L \int_0^b \bar{D}_{g2,11} [(\delta \kappa_{g2,zz}^{bL})^2 + \kappa_{pg2,zz} \delta^2 \kappa_{g2,zz}^{bN}] dx dz + \int_0^L \int_0^b \bar{A}_{g2,66} (\delta \gamma_{g2,sz}^{bL})^2 dx dz \\
& \left. + \int_0^L \int_0^b \bar{D}_{g2,66} (\delta \kappa_{g2,sz}^{bL})^2 dx dz + \int_0^L \int_{A_{a2}} G_{a2} (\delta \gamma_{a2,zn}^{bL})^2 dA_{a2} dz + \int_0^L \int_{A_{a2}} G_{a2} (\delta \gamma_{a2,sn}^{bL})^2 dA_{a2} dz + \int_0^L \int_{A_{a2}} G_{a2} (\delta \gamma_{a2,sz}^{bL})^2 dA_{a2} dz \right].
\end{aligned} \tag{27}$$

The second variation of the total load potential loss in Eq. (25) causes loads $P_y(z_p, y_p)$ and $q_y(z_q, y_q)$ and can be obtained as

$$\begin{aligned}
\frac{1}{2} \delta^2 V = & \frac{1}{2} \left[-P_y(z_p, y_p) \cdot y_p \cdot [\delta \theta_{zb}(z_p)]^2 \right. \\
& \left. - \int_0^L q_y(z_q, y_q) \cdot y_q \cdot [\delta \theta_{zb}(z_q)]^2 dz \right].
\end{aligned} \tag{28}$$

In Eq. (27), pre-buckling strains ε_{ps} , γ_{ps} , $\varepsilon_{pg1,zz}$, $\kappa_{pg1,zz}$, $\varepsilon_{pg2,zz}$, and $\kappa_{pg2,zz}$ have been defined in Eq. (24). Meanwhile,

the strains with superscript bL in Eq. (27) denote the first variation of linear buckling strains, while those with superscript bN denote the second variation of nonlinear buckling strains.

3.6.1 First variation of linear buckling strains

The linear buckling strains in Eq. (27) can be obtained by neglecting pre-buckling and high-order terms in Eqs. (9)–(17) and taking the first variation. As a result, we obtain

$$\begin{aligned}
\delta \varepsilon_s^{bL} &= -n_s \sin \alpha(s_s) \delta U_b''(z) - x(s_s) \delta \theta_{yb}'(z) + n_s q(s_s) \delta \theta_{zb}''(z) - \omega(s_s) \delta \psi_b'(z), \\
\delta \gamma_{s,sz}^{bL} &= \cos \alpha(s_s) \delta U_b'(z) - \cos \alpha(s_s) \delta \theta_{yb}(z) + [r(s_s) + 2n_1] \delta \theta_{zb}'(z) - r(s_s) \delta \psi_b(z), \\
\delta \varepsilon_{g1,zz}^{bL} &= -x(s_{g1}) \delta \theta_{y1b}(z), \quad \delta \kappa_{g1,zz}^{bL} = x(s_{g1}) \delta \theta_{zb}''(z), \delta \gamma_{g1,sz}^{bL} = \delta U_{1b}'(z) - \delta \theta_{y1b}(z), \quad \delta \kappa_{g1,sz}^{bL} = 2 \delta \theta_{zb}'(z), \\
\delta \gamma_{a1,zn}^{bL} &= \frac{1}{t_{a1}} x(s_{a1}) \delta \theta_{yb}(z) - \frac{1}{t_{a1}} x(s_{a1}) \delta \theta_{y1b}(z) - \left[\frac{t_f + t_{g1}}{2t_{a1}} + 1 \right] x(s_{a1}) \delta \theta_{zb}'(z) + \frac{h_b}{2t_{a1}} x(s_{a1}) \delta \psi_b(z), \\
\delta \gamma_{a1,sn}^{bL} &= -\frac{1}{t_{a1}} \delta U_b(z) + \frac{1}{t_{a1}} \delta U_{1b}(z) - \left[1 + \frac{h + t_{g1}}{2t_{a1}} \right] \delta \theta_{zb}(z), \\
\delta \gamma_{a1,sz}^{bL} &= \left(\frac{1}{2} - \frac{n_{a1}}{t_{a1}} \right) \delta U_b'(z) - \left(\frac{1}{2} - \frac{n_{a1}}{t_{a1}} \right) \delta \theta_{yb}(z) + \left(\frac{1}{2} + \frac{n_{a1}}{t_{a1}} \right) \delta U_{1b}'(z) - \left(\frac{1}{2} + \frac{n_{a1}}{t_{a1}} \right) \delta \theta_{y1b}(z) \\
&\quad + \left[\frac{h + t_f - 2t_{g1}}{4} - \frac{(h + t_f + 2t_{g1})n_{a1}}{2t_{a1}} \right] \delta \theta_{zb}'(z) - \frac{h_b}{2} \left(\frac{1}{2} - \frac{n_{a1}}{t_{a1}} \right) \delta \psi_b(z) \quad (29) \\
\delta \varepsilon_{g2,zz}^{bL} &= -x(s_{g2}) \delta \theta_{y2b}'(z), \quad \delta \kappa_{g2,zz}^{bL} = +x(s_{g2}) \delta \theta_{zb}''(z), \quad \delta \gamma_{g2,sz}^{bL} = -\delta \theta_{y2b}(z) + \delta U_{2b}'(z), \quad \delta \kappa_{g2,sz}^{bL} = 2 \delta \theta_{zb}'(z), \\
\delta \gamma_{a2,zn}^{bL} &= -\frac{1}{t_{a2}} x(s_{a2}) \delta \theta_{yb} + \frac{1}{t_{a2}} x(s_{a2}) \delta \theta_{y2b}(z) - \left[\frac{(t_f + t_{g2})}{2t_{a2}} + 1 \right] x(s_{a2}) \delta \theta_{zb}'(z) + \frac{h_b}{2t_{a2}} x(s_{a2}) \delta \psi_b(z), \\
\delta \gamma_{a2,sn}^{bL} &= -\frac{\delta U_{2b}(z)}{t_{a2}} + \frac{\delta U_b(z)}{t_{a2}} - \left(\frac{h + t_{g2}}{2t_{a2}} + 1 \right) \delta \theta_{zb}(z), \\
\delta \gamma_{a2,sz}^{bL} &= \left(\frac{1}{2} + \frac{n_{a2}}{t_{a2}} \right) \delta U_b'(z) - \left(\frac{1}{2} + \frac{n_{a2}}{t_{a2}} \right) \delta \theta_{yb}(z) + \left(\frac{1}{2} - \frac{n_{a2}}{t_{a2}} \right) \delta U_{2b}'(z) \\
&\quad - \left(\frac{1}{2} - \frac{n_{a2}}{t_{a2}} \right) \delta \theta_{y2b}(z) - \left[\frac{t_f + h - 2t_{g2}}{4} + \frac{(t_f + h + 2t_{g2})n_{a2}}{2t_{a2}} \right] \delta \theta_{zb}'(z) + \frac{h_b}{2} \left(\frac{1}{2} + \frac{n_{a2}}{t_{a2}} \right) \delta \psi_b(z).
\end{aligned}$$

3.6.2 Second variation of nonlinear buckling strains

The second variation of nonlinear buckling strains is evaluated by neglecting linear terms from Eqs. (9)–(17). Taking the second variation and neglecting high-order terms, we have

$$\begin{aligned}
\delta^2 \varepsilon_s^{*bN} &= (\delta U_b')^2 + 2[n_s \cos \alpha(s_s) - y(s_s)] \delta U_b'(z) \delta \theta_{zb}'(z) + \{q^2(s_s) + [r(s_s) + n_s]^2\} (\delta \theta_{zb}')^2, \\
\delta^2 \gamma_{s,sz}^{bN} &= -2 \sin \alpha(s_s) \delta U_b'(z) \delta \theta_{zb}(z) - 2n_s^2 \sin \alpha(s_s) U_b''(z) \theta_{zb}'(z), \quad \delta^2 \varepsilon_{g1}^{bN} \approx (\delta U_{1b}')^2 + x^2(s) (\delta \theta_{zb}')^2, \\
\delta^2 \kappa_{g1}^{bN} &\approx 2 \delta U_{1b}' \delta \theta_{zb}'(z), \quad \delta^2 \varepsilon_{g2}^{bN} \approx (\delta U_{2b}')^2 + x^2(s) (\delta \theta_{zb}')^2, \quad \delta^2 \kappa_{g2}^{bN} \approx 2 \delta U_{2b}' \delta \theta_{zb}'(z). \quad (30)
\end{aligned}$$

3.6.3 Buckling energy expressions

From Eqs. (24), (27), (29), and (30), by substituting into Eq. (25), the second variation of the strain energy is finally obtained. By taking integrals over the sectional areas, one obtains

$$\begin{aligned}
\frac{1}{2}\delta^2\pi = & \frac{1}{2}\int_0^L [E_s[I_{s,yyw}\delta U_b''(z)\delta U_b''(z) + 2I_{s,yyf}\delta\theta_{yb}'(z)\delta\theta_{yb}'(z) + I_{s,\omega\omega l}\delta\theta_{zb}''(z)\delta\theta_{zb}''(z) + I_{s,\omega\omega g}\delta\psi_b'(z)\delta\psi_b'(z)]dz \\
& + \int_0^L \langle \delta U_b'(z) \quad \delta\theta_{yb}(z) \quad \delta\theta_{zb}'(z) \quad \delta\psi_b(z) \rangle G_s \begin{bmatrix} 2A_f & -2A_f & 0 & 0 \\ -2A_f & 2A_f & 0 & 0 \\ 0 & 0 & J_1 & -h_b^2 A_f/2 \\ 0 & 0 & -h_b^2 A_f/2 & h_b^2 A_f/2 \end{bmatrix} \begin{bmatrix} \delta U_b'(z) \\ \delta\theta_{yb}(z) \\ \delta\theta_{zb}'(z) \\ \delta\psi_b(z) \end{bmatrix} dz + \int_0^L \delta\theta_{y1b}'(z)(\bar{A}_{g1,11}b^3/12)\delta\theta_{y1b}(z)dz \\
& + \int_0^L \delta\theta_{zb}'(z)(\bar{D}_{g1,11}b^3/12)\delta\theta_{zb}'(z)dz + \int_0^L \langle \delta U_{1b}'(z) \quad \delta\theta_{y1b}(z) \rangle \bar{A}_{g1,66}b \begin{bmatrix} 1 & -1 \\ -1 & 1 \end{bmatrix} \begin{bmatrix} \delta U_{1b}'(z) \\ \delta\theta_{y1b}(z) \end{bmatrix} dz + \int_0^L \delta\theta_{zb}'(z)(4b\bar{D}_{g1,66})\delta\theta_{zb}'(z)dz \\
& + G_{a1}\int_0^L \frac{b^3}{48t_{a1}} \langle \delta\theta_{yb}(z) \quad \delta\theta_{y1b}(z) \quad \delta\theta_{zb}'(z) \quad \delta\psi_b(z) \rangle \begin{bmatrix} 4 & -4 & -2t_{fga1} & 2h_b \\ -4 & 4 & 2t_{fga1} & -2h_b \\ -2t_{fga1} & 2t_{fga1} & t_{fga1}^2 & -h_b t_{fga1} \\ 2h_b & -2h_b & -h_b t_{fga1} & h_b^2 \end{bmatrix} \begin{bmatrix} \delta\theta_{yb}(z) \\ \delta\theta_{y1b}(z) \\ \delta\theta_{zb}'(z) \\ \delta\psi_b(z) \end{bmatrix} dz \\
& + G_{a1}\int_0^L \langle \delta U_b(z) \quad \delta\theta_{zb}(z) \quad \delta U_{1b}(z) \rangle \chi_{a1,a} \begin{bmatrix} 4 & 2d_{a1,o} & -4 \\ 2d_{a1,o} & d_{a1,o}^2 & -2d_{a1,o} \\ -4 & -2d_{a1,o} & 4 \end{bmatrix} \begin{bmatrix} \delta U_b(z) \\ \delta\theta_{zb}(z) \\ \delta U_{1b}(z) \end{bmatrix} dz \\
& + G_{a1}\int_0^L \langle \delta U_b'(z) \quad \delta\theta_{yb}(z) \quad \delta U_{1b}'(z) \quad \delta\theta_{y1b}(z) \quad \delta\theta_{zb}'(z) \quad \delta\psi_b(z) \rangle \\
& \times \frac{bt_{a1}}{6} \begin{bmatrix} 2 & -2 & 1 & -1 & h_{1sz1} & -h_b \\ -2 & 2 & -1 & 1 & -h_{1sz1} & h_b \\ 1 & -1 & 2 & -2 & h_{2sz1} & -h_b/2 \\ -1 & 1 & -2 & 2 & -h_{2sz1} & h_b/2 \\ h_{1sz1} & -h_{1sz1} & h_{2sz1} & -h_{2sz1} & h_{3sz1} & -h_b h_{1sz1}/2 \\ -h_b & h_b & -h_b/2 & h_b/2 & -h_b h_{1sz1}/2 & h_b^2/2 \end{bmatrix} \begin{bmatrix} \delta U_b'(z) \\ \delta\theta_{yb}(z) \\ \delta U_{1b}'(z) \\ \delta\theta_{y1b}(z) \\ \delta\theta_{zb}'(z) \\ \delta\psi_b(z) \end{bmatrix} dz \\
& + \int_0^L \delta\theta_{y2b}'(z)(\bar{A}_{g2,11}b^3/12)\delta\theta_{y2b}'(z)dz + \int_0^L \delta\theta_{zb}'(z)(\bar{D}_{g2,11}b^3/12)\delta\theta_{zb}'(z)dz \\
& + \int_0^L \langle \delta U_{2b}'(z) \quad \delta\theta_{y2b}(z) \rangle \bar{A}_{g2,66}b \begin{bmatrix} 1 & -1 \\ -1 & 1 \end{bmatrix} \begin{bmatrix} \delta U_{2b}'(z) \\ \delta\theta_{y2b}(z) \end{bmatrix} dz + \int_0^L \delta\theta_{zb}'(z)(4b\bar{D}_{g2,66})\delta\theta_{zb}'(z)dz \\
& + G_{a2}\int_0^L \frac{b^3}{48t_{a2}} \langle \delta\theta_{yb}(z) \quad \delta\theta_{y2b}(z) \quad \delta\theta_{zb}'(z) \quad \delta\psi_b(z) \rangle \\
& \times \begin{bmatrix} 4 & -4 & 2t_{fga2} & -2h_b \\ -4 & 4 & -2t_{fga2} & 2h_b \\ 2t_{fga2} & -2t_{fga2} & t_{fga2}^2 & -h_b t_{fga2} \\ -2h_b & 2h_b & -h_b t_{fga2} & h_b^2 \end{bmatrix} \begin{bmatrix} \delta\theta_{yb}(z) \\ \delta\theta_{y2b}(z) \\ \delta\theta_{zb}'(z) \\ \delta\psi_b(z) \end{bmatrix} dz + G_{a2}\int_0^L \langle \delta U_b(z) \quad \delta\theta_{zb}(z) \quad \delta U_{2b}(z) \rangle \chi_{a2,a} \\
& \times \begin{bmatrix} 4 & -2d_{a2,o} & -4 \\ -2d_{a2,o} & d_{a2,o}^2 & 2d_{a2,o} \\ -4 & 2d_{a2,o} & 4 \end{bmatrix} \begin{bmatrix} \delta U_b(z) \\ \delta\theta_{zb}(z) \\ \delta U_{2b}(z) \end{bmatrix} dz + G_{a2}\int_0^L \langle \delta U_b'(z) \quad \delta\theta_{yb}(z) \quad \delta U_{2b}'(z) \quad \delta\theta_{y2b}(z) \quad \delta\theta_{zb}'(z) \quad \delta\psi_b(z) \rangle \\
& \times \frac{bt_{a2}}{6} \begin{bmatrix} 2 & -2 & 1 & -1 & -h_{1sz2} & h_b \\ -2 & 2 & -1 & 1 & h_{1sz2} & -h_b \\ 1 & -1 & 2 & -2 & -h_{2sz2} & h_b/2 \\ -1 & 1 & -2 & 2 & h_{2sz2} & -h_b/2 \\ -h_{1sz2} & h_{1sz2} & -h_{2sz2} & h_{2sz2} & h_{3sz2} & -h_b h_{1sz2}/2 \\ h_b & -h_b & h_b/2 & -h_b/2 & -h_b h_{1sz2}/2 & h_b^2/2 \end{bmatrix} \begin{bmatrix} \delta U_b'(z) \\ \delta\theta_{yb}(z) \\ \delta U_{2b}'(z) \\ \delta\theta_{y2b}(z) \\ \delta\theta_{zb}'(z) \\ \delta\psi_b(z) \end{bmatrix} dz \\
& + 2\int_0^L M_{xsp}(z)\delta U_b'\delta\theta_{yb}'dz - 2\int_0^L Q_p(z)\delta U_b'(z)\delta\theta_{zb}(z)dz + \int_0^L N_p(z)[(\delta U_b')^2 + ((I_{s,xx} + I_{s,yy})/A_s)(\delta\theta_{zb}')^2]dz \\
& + \int_0^L N_{1p}[(\delta U_{1b}')^2 + \frac{b^2}{12}(\delta\theta_{y1b}'(z))^2]dz + \int_0^L N_{2p}[(\delta U_{2b}')^2 + \frac{b^2}{12}(\delta\theta_{y2b}'(z))^2]dz \\
& + \frac{1}{2}\left[-P_y(z_p, y_p) \cdot y_p \cdot [\delta\theta_{zb}(z_p)]^2 - \int_0^L q_y(z_q, y_q) \cdot y_q \cdot [\delta\theta_{zb}(z_q)]^2 dz\right],
\end{aligned} \tag{31}$$

where the sectional properties in Eq. (31) are defined as

$$\begin{aligned}
 I_{yyw} &= h_w t_w^3/12, \quad I_{yyf} = t_f b^3/12, \quad I_{\omega\omega l} = 2b^3 t_f^3/144 + h_w^3 t_w^3/144, \quad I_{\omega\omega gs} = h_b^2 b^3 t_f/24, \quad A_f = bt, \\
 J_1 &= h_b^2 A_f/2 + 2bt^3/3 + h_w t_w^3/3, \quad t_{fga1} = t_f + t_{g1} + 2t_{a1}, \quad d_{a1,o} = h + 2t_{a1} + t_{g1}, \quad \chi_{a1,a} = A_{a1,a} a_{a1,o}, \\
 a_{a1,o} &= 1/4t_{a1}^2, \quad h_{1sz1} = h + t_f - t_{g1}, \quad h_{2sz1} = (h + t_f)/2 - 2t_{g1}, \quad h_{3sz1} = h^2/2 + t_f^2/2 + 2t_{g1}^2 + ht_f - ht_{g1} - t_f t_{g1}, \\
 t_{fga2} &= t_f + t_{g2} + 2t_{a2}, \quad h_{1sz2} = h + t_f - t_{g2}, \quad h_{2sz2} = (h + t_f)/2 - 2t_{g2}, \\
 h_{3sz2} &= h^2/2 + t_f^2/2 + 2t_{g2}^2 + ht_f - ht_{g2} - t_f t_{g2}, \quad d_{a2,o} = h + 2t_{a2} + t_{g2}, \quad \chi_{a2,a} = A_{a2,a} a_{a2,o}; \quad a_{a2,o} = 1/4t_{a2}^2,
 \end{aligned} \tag{32}$$

while material properties $E_s, G_s, G_{a1}, \bar{A}_{g1,11}, \bar{A}_{g1,66}, \bar{D}_{g1,11}, \bar{D}_{g1,66}, G_{a2}, \bar{A}_{g2,11}, \bar{A}_{g2,66}, \bar{D}_{g2,11}, \bar{D}_{g2,66}$ are given in Section 3.4.

3.7 Development of an FE formulation

An FE formulation is developed for the FRP-strengthened steel beam, as defined in Figure 1a and b. An approximation of the governing displacement fields is assumed as

$$\begin{aligned}
 &\langle U_b(z) \ \theta_{yb}(z) \ \theta_{zb}(z) \ \psi_b(z) \ \theta_{y1b}(z) \ U_{1b}(z) \ \theta_{y2b}(z) \ U_{2b}(z) \rangle_{1 \times 8}^T \\
 &= \langle \Delta \rangle_{1 \times 20}^T \langle \{Z_u\}_{20 \times 1} \ \{Z_{\theta y}\}_{20 \times 1} \ \{Z_{\theta z}\}_{20 \times 1} \ \{Z_{\psi}\}_{20 \times 1} \ \{Z_{\theta y1}\}_{20 \times 1} \ \{Z_{u1}\}_{20 \times 1} \ \{Z_{\theta y2}\}_{20 \times 1} \ \{Z_{u2}\}_{20 \times 1} \rangle_{20 \times 8},
 \end{aligned} \tag{33}$$

where $\{\Delta\}_{20 \times 1}$ is the element nodal displacement vector that is expressed as

$$\begin{aligned}
 \langle \Delta \rangle_{1 \times 20}^T &= \langle U_{b,0} \ U'_{b,0} \ \theta_{yb,0} \ \theta_{zb,0} \ \theta'_{zb,0} \ \psi_{b,0} \ \theta_{y1b,0} \ U_{1b,0} \ \theta_{y2b,0} \ U_{2b,0} \\
 &\quad U_{b,L} \ U'_{b,L} \ \theta_{yb,L} \ \theta_{zb,L} \ \theta'_{zb,L} \ \psi_{b,L} \ \theta_{y1b,L} \ U_{1b,L} \ \theta_{y2b,L} \ U_{2b,L} \rangle',
 \end{aligned} \tag{34}$$

in which the governing displacements with subscript 0 denote the nodal displacement at coordinate $Z = 0$ of the element, while those with subscript L denote the nodal displacement at coordinate of the element. The shape functions in Eq. (33) are defined as

$$\begin{aligned}
 \langle Z_u \rangle_{1 \times 20}^T &= \langle f_1(z) \ f_2(z) \ 0 \ 0 \ 0 \ 0 \ 0 \ 0 \ 0 \ 0 \ f_3(z) \ f_4(z) \ 0 \ 0 \ 0 \ 0 \ 0 \ 0 \ 0 \rangle, \\
 \langle Z_{\theta y} \rangle_{1 \times 20}^T &= \langle 0 \ 0 \ f_5(z) \ 0 \ 0 \ 0 \ 0 \ 0 \ 0 \ 0 \ 0 \ f_6(z) \ 0 \ 0 \ 0 \ 0 \ 0 \ 0 \ 0 \rangle, \\
 \langle Z_{\theta z} \rangle_{1 \times 20}^T &= \langle 0 \ 0 \ 0 \ f_1(z) \ f_2(z) \ 0 \ 0 \ 0 \ 0 \ 0 \ 0 \ 0 \ 0 \ f_3(z) \ f_4(z) \ 0 \ 0 \ 0 \ 0 \ 0 \rangle, \\
 \langle Z_{\psi} \rangle_{1 \times 20}^T &= \langle 0 \ 0 \ 0 \ 0 \ 0 \ f_5(z) \ 0 \ 0 \ 0 \ 0 \ 0 \ 0 \ 0 \ 0 \ f_6(z) \ 0 \ 0 \ 0 \ 0 \rangle, \\
 \langle Z_{\theta y1} \rangle_{1 \times 20}^T &= \langle 0 \ 0 \ 0 \ 0 \ 0 \ 0 \ f_5(z) \ 0 \ 0 \ 0 \ 0 \ 0 \ 0 \ 0 \ 0 \ f_6(z) \ 0 \ 0 \ 0 \rangle, \\
 \langle Z_{u1} \rangle_{1 \times 20}^T &= \langle 0 \ 0 \ 0 \ 0 \ 0 \ 0 \ 0 \ f_5(z) \ 0 \ 0 \ 0 \ 0 \ 0 \ 0 \ 0 \ 0 \ f_6(z) \ 0 \ 0 \rangle, \\
 \langle Z_{\theta y2} \rangle_{1 \times 20}^T &= \langle 0 \ 0 \ 0 \ 0 \ 0 \ 0 \ 0 \ 0 \ f_5(z) \ 0 \ 0 \ 0 \ 0 \ 0 \ 0 \ 0 \ 0 \ f_6(z) \ 0 \rangle, \\
 \langle Z_{u2} \rangle_{1 \times 20}^T &= \langle 0 \ 0 \ 0 \ 0 \ 0 \ 0 \ 0 \ 0 \ 0 \ f_5(z) \ 0 \ 0 \ 0 \ 0 \ 0 \ 0 \ 0 \ 0 \ f_6(z) \rangle,
 \end{aligned} \tag{35}$$

in which the following approximate functions of z coordinates are given as

$$\begin{aligned} f_1(z) &= 1 - 3(z/L)^2 + 2(z/L)^3, \\ f_3(z) &= 3(z/L)^2 - 2(z/L)^3, \quad f_5(z) = 1 - z/L, \\ f_2(z) &= z - 2(z^2/L) + (z^3/L^2), \\ f_4(z) &= z^3/L^2 - z^2/L, \quad f_6(z) = z/L. \end{aligned} \quad (36)$$

Based on the total pre-buckling potential energy as developed in Section 3.5, an FE formulation can be developed to predict the static responses (*i.e.*, stress resultants and displacements) of the system. This work was completed by Thanh and Phe [41]. The pre-buckling stress results can be obtained and expressed as

$$\begin{aligned} N_p(z) &= \langle \mathbf{Z}_p \rangle_{1 \times 2} \{ \mathbf{N}_p \}_{2 \times 1}; \\ M_{xsp}(z) &= \langle \mathbf{Z}_p \rangle_{1 \times 2} \{ \mathbf{M}_{xsp} \}_{2 \times 1}; \\ Q_p(z) &= \langle \mathbf{Z}_p \rangle_{1 \times 2} \{ \mathbf{Q}_p \}_{2 \times 1} \\ N_{1p}(z) &= \langle \mathbf{Z}_p \rangle_{1 \times 2} \{ \mathbf{N}_{1p} \}_{2 \times 1}; \\ N_{2p}(z) &= \langle \mathbf{Z}_p \rangle_{1 \times 2} \{ \mathbf{N}_{2p} \}_{2 \times 1}, \end{aligned} \quad (37)$$

in which the following nodal pre-buckling stress results are defined as

$$\begin{aligned} \langle \mathbf{N}_p \rangle_{1 \times 2}^T &= \langle N_{p,0} \quad N_{p,L} \rangle, \\ \langle \mathbf{M}_{xsp} \rangle_{1 \times 2}^T &= \langle M_{xsp,0} M_{xsp,L} \rangle, \\ \langle \mathbf{Q}_p \rangle_{1 \times 2}^T &= \langle Q_{p,0} \quad Q_{p,L} \rangle \\ \langle \mathbf{N}_{1p} \rangle_{1 \times 2}^T &= \langle N_{1p,L} \rangle, \\ \langle \mathbf{N}_{2p} \rangle_{1 \times 2}^T &= \langle N_{2p,0} \quad N_{2p,L} \rangle. \end{aligned} \quad (38)$$

In Eq. (38), the nodal forces with subscript 0 denote those at coordinate $z = 0$, while the nodal forces with subscript L denote those at $z = L$. Also, $\langle \mathbf{Z}_p \rangle_{1 \times 2} = \langle f_5(z) \quad f_6(z) \rangle$, where $f_5(z)$, $f_6(z)$ are defined in Eq. (36). From Eqs. (33) and (37), by substituting into Eq. (31) and applying the condition of buckling equilibrium as presented in Eq. (25), an FE formulation for the buckling problem (*i.e.*, an eigenvalue problem) can be obtained as

$$\{ [\mathbf{K}_E]_{20 \times 20} + \lambda [\mathbf{K}_G]_{20 \times 20} \} \{ \Delta \}_{20 \times 1} = \{ \mathbf{0} \}_{20 \times 1}, \quad (39)$$

in which $[\mathbf{K}_E]_{20 \times 20}$ is the elastic stiffness matrix and $[\mathbf{K}_G]_{20 \times 20}$ is the geometric stiffness matrix of the element. They are obtained as

$$\begin{aligned} [\mathbf{K}_E]_{20 \times 20} &= \int_0^L \{ E_s I_{s,yy} \{ \mathbf{Z}_u'' \}_{20 \times 1} \langle \mathbf{Z}_u'' \rangle_{1 \times 20}^T + 2 E_s I_{s,yyf} \{ \mathbf{Z}_{\theta y}' \}_{20 \times 1} \langle \mathbf{Z}_{\theta y}' \rangle_{1 \times 20}^T + E_s I_{s,\omega\omega} \{ \mathbf{Z}_{qz}'' \}_{20 \times 1} \langle \mathbf{Z}_{qz}'' \rangle_{1 \times 20}^T \\ &\quad + E_s I_{s,\omega\omega g} \{ \mathbf{Z}_{\psi}' \}_{20 \times 1} \langle \mathbf{Z}_{\psi}' \rangle_{1 \times 20}^T + \langle \{ \mathbf{Z}_u' \}_{20 \times 1} \quad \{ \mathbf{Z}_{\theta y}' \}_{20 \times 1} \quad \{ \mathbf{Z}_{qz}' \}_{20 \times 1} \quad \{ \mathbf{Z}_{\psi}' \}_{20 \times 1} \rangle \\ &\quad \times G_s \begin{bmatrix} 2A_f & -2A_f & 0 & 0 \\ -2A_f & 2A_f & 0 & 0 \\ 0 & 0 & J_1 & -h_b^2 A_f / 2 \\ 0 & 0 & -h_b^2 A_f / 2 & h_b^2 A_f / 2 \end{bmatrix} \begin{bmatrix} \langle \mathbf{Z}_u' \rangle_{1 \times 20}^T \\ \langle \mathbf{Z}_{\theta y}' \rangle_{1 \times 20}^T \\ \langle \mathbf{Z}_{qz}' \rangle_{1 \times 20}^T \\ \langle \mathbf{Z}_{\psi}' \rangle_{1 \times 20}^T \end{bmatrix} + \{ \mathbf{Z}_{qy1}' \}_{20 \times 1} (\bar{A}_{g1,11} b^3 / 12) \langle \mathbf{Z}_{qy1}' \rangle_{1 \times 20}^T \\ &\quad + \{ \mathbf{Z}_{qz}'' \}_{20 \times 1} (\bar{D}_{g1,11} b^3 / 12) \langle \mathbf{Z}_{qz}'' \rangle_{1 \times 20}^T + \{ \mathbf{Z}_{qz}' \}_{20 \times 1} (4b \bar{D}_{g1,66}) \langle \mathbf{Z}_{qz}' \rangle_{1 \times 20}^T + \{ \mathbf{Z}_{qy2}' \}_{20 \times 1} (\bar{A}_{g2,11} b^3 / 12) \langle \mathbf{Z}_{qy2}' \rangle_{1 \times 20}^T \\ &\quad + \{ \mathbf{Z}_{qz}'' \}_{20 \times 1} (\bar{D}_{g2,11} b^3 / 12) \langle \mathbf{Z}_{qz}'' \rangle_{1 \times 20}^T + \{ \mathbf{Z}_{qz}' \}_{20 \times 1} (4b \bar{D}_{g2,66}) \langle \mathbf{Z}_{qz}' \rangle_{1 \times 20}^T + \langle \{ \mathbf{Z}_{u1}' \}_{20 \times 1} \quad \{ \mathbf{Z}_{qy1}' \}_{20 \times 1} \rangle \\ &\quad \times \bar{A}_{g1,66} b \begin{bmatrix} 1 & -1 \\ -1 & 1 \end{bmatrix} \begin{bmatrix} \langle \mathbf{Z}_{u1}' \rangle_{1 \times 20}^T \\ \langle \mathbf{Z}_{qy1}' \rangle_{1 \times 20}^T \end{bmatrix} + \langle \{ \mathbf{Z}_{u2}' \}_{20 \times 1} \quad \{ \mathbf{Z}_{qy2}' \}_{20 \times 1} \rangle \bar{A}_{g2,66} b \begin{bmatrix} 1 & -1 \\ -1 & 1 \end{bmatrix} \begin{bmatrix} \langle \mathbf{Z}_{u2}' \rangle_{1 \times 20}^T \\ \langle \mathbf{Z}_{qy2}' \rangle_{1 \times 20}^T \end{bmatrix} \\ &\quad + G_{a1} \frac{b^3}{48 t_{a1}} \langle \{ \mathbf{Z}_{\theta y}' \}_{20 \times 1} \quad \{ \mathbf{Z}_{qy1}' \}_{20 \times 1} \quad \{ \mathbf{Z}_{qz}' \}_{20 \times 1} \quad \{ \mathbf{Z}_{\psi}' \}_{20 \times 1} \rangle \begin{bmatrix} 4 & -4 & -2t_{fga1} & 2h_b \\ -4 & 4 & 2t_{fga1} & -2h_b \\ -2t_{fga1} & 2t_{fga1} & t_{fga1}^2 & -h_b t_{fga1} \\ 2h_b & -2h_b & -h_b t_{fga1} & h_b^2 \end{bmatrix} \begin{bmatrix} \langle \mathbf{Z}_{\theta y}' \rangle_{1 \times 20}^T \\ \langle \mathbf{Z}_{qy1}' \rangle_{1 \times 20}^T \\ \langle \mathbf{Z}_{qz}' \rangle_{1 \times 20}^T \\ \langle \mathbf{Z}_{\psi}' \rangle_{1 \times 20}^T \end{bmatrix} \\ &\quad + G_{a1} \langle \{ \mathbf{Z}_{u1}' \}_{20 \times 1} \quad \{ \mathbf{Z}_{qz}' \}_{20 \times 1} \quad \{ \mathbf{Z}_{u1}' \}_{20 \times 1} \rangle \times \chi_{a1,a} \begin{bmatrix} 4 & 2d_{a1,o} & -4 \\ 2d_{a1,o} & d_{a1,o}^2 & -2d_{a1,o} \\ -4 & -2d_{a1,o} & 4 \end{bmatrix} \begin{bmatrix} \langle \mathbf{Z}_{u1}' \rangle_{1 \times 20}^T \\ \langle \mathbf{Z}_{qz}' \rangle_{1 \times 20}^T \\ \langle \mathbf{Z}_{u1}' \rangle_{1 \times 20}^T \end{bmatrix} \end{aligned} \quad (40)$$

$$\begin{aligned}
& + G_{a1} \int_0^L \langle \{Z'_u\}_{20 \times 1} \{Z_{\theta y}\}_{20 \times 1} \{Z'_{u1}\}_{20 \times 1} \{Z_{qy1}\}_{20 \times 1} \{Z'_{qz}\}_{20 \times 1} \{Z_{\psi}\}_{20 \times 1} \rangle \\
& \times \frac{bt_{a1}}{6} \begin{bmatrix} 2 & -2 & 1 & -1 & h_{1sz1} & -h_b \\ -2 & 2 & -1 & 1 & -h_{1sz1} & h_b \\ 1 & -1 & 2 & -2 & h_{2sz1} & -h_b/2 \\ -1 & 1 & -2 & 2 & -h_{2sz1} & h_b/2 \\ h_{1sz1} & -h_{1sz1} & h_{2sz1} & -h_{2sz1} & h_{3sz1} & -h_b h_{1sz1}/2 \\ -h_b & h_b & -h_b/2 & h_b/2 & -h_b h_{1sz1}/2 & h_b^2/2 \end{bmatrix} \begin{bmatrix} \langle Z'_u \rangle_{1 \times 20}^T \\ \langle Z_{\theta y} \rangle_{1 \times 20}^T \\ \langle Z'_{u1} \rangle_{1 \times 20}^T \\ \langle Z_{qy1} \rangle_{1 \times 20}^T \\ \langle Z'_{qz} \rangle_{1 \times 20}^T \\ \langle Z_{\psi} \rangle_{1 \times 20}^T \end{bmatrix} \\
& + \frac{G_{a2} b^3}{48 t_{a2}} \langle \{Z_{\theta y}\}_{20 \times 1} \{Z_{qy2}\}_{20 \times 1} \{Z'_{qz}\}_{20 \times 1} \{Z_{\psi}\}_{20 \times 1} \rangle \times \begin{bmatrix} 4 & -4 & 2t_{fga2} & -2h_b \\ -4 & 4 & -2t_{fga2} & 2h_b \\ 2t_{fga2} & -2t_{fga2} & t_{fga2}^2 & -h_b t_{fga2} \\ -2h_b & 2h_b & -h_b t_{fga2} & h_b^2 \end{bmatrix} \begin{bmatrix} \langle Z_{\theta y} \rangle_{1 \times 20}^T \\ \langle Z_{qy2} \rangle_{1 \times 20}^T \\ \langle Z'_{qz} \rangle_{1 \times 20}^T \\ \langle Z_{\psi} \rangle_{1 \times 20}^T \end{bmatrix} \\
& + G_{a2} \langle \{Z_u\}_{20 \times 1} \{Z_{qz}\}_{20 \times 1} \{Z_{u2}\}_{20 \times 1} \rangle \times \chi_{a2,a} \begin{bmatrix} 4 & -2d_{a2,o} & -4 \\ -2d_{a2,o} & d_{a2,o}^2 & 2d_{a2,o} \\ -4 & 2d_{a2,o} & 4 \end{bmatrix} \begin{bmatrix} \langle Z_u \rangle_{1 \times 20}^T \\ \langle Z_{qz} \rangle_{1 \times 20}^T \\ \langle Z_{u2} \rangle_{1 \times 20}^T \end{bmatrix} \\
& + G_{a2} \langle \{Z'_u\}_{20 \times 1} \{Z_{\theta y}\}_{20 \times 1} \{Z'_{u2}\}_{20 \times 1} \{Z_{qy2}\}_{20 \times 1} \{Z'_{qz}\}_{20 \times 1} \{Z_{\psi}\}_{20 \times 1} \rangle \\
& \times \frac{bt_{a2}}{6} \begin{bmatrix} 2 & -2 & 1 & -1 & -h_{1sz2} & h_b \\ -2 & 2 & -1 & 1 & h_{1sz2} & -h_b \\ 1 & -1 & 2 & -2 & -h_{2sz2} & h_b/2 \\ -1 & 1 & -2 & 2 & h_{2sz2} & -h_b/2 \\ -h_{1sz2} & h_{1sz2} & -h_{2sz2} & h_{2sz2} & h_{3sz2} & -h_b h_{1sz2}/2 \\ h_b & -h_b & h_b/2 & -h_b/2 & -h_b h_{1sz2}/2 & h_b^2/2 \end{bmatrix} \begin{bmatrix} \langle Z'_u \rangle_{1 \times 20}^T \\ \langle Z_{\theta y} \rangle_{1 \times 20}^T \\ \langle Z'_{u2} \rangle_{1 \times 20}^T \\ \langle Z_{qy2} \rangle_{1 \times 20}^T \\ \langle Z'_{qz} \rangle_{1 \times 20}^T \\ \langle Z_{\psi} \rangle_{1 \times 20}^T \end{bmatrix} dz,
\end{aligned}$$

and

$$\begin{aligned}
[K_G]_{12 \times 12} = & \int_0^L \left[\langle N_p \rangle_{1 \times 2} \{Z_p\}_{2 \times 1} \{ \{Z'_{ub}\}_{20 \times 1} \langle Z'_{ub} \rangle_{1 \times 20}^T + \frac{I_{s,xx} + I_{s,yy}}{A_s} \{Z_{\theta z}\}_{20 \times 1} \langle Z_{\theta z} \rangle_{1 \times 20}^T \right] dz - \langle Q_p \rangle_{1 \times 2} \{Z_p\}_{2 \times 1} \{ \{Z'_{ub}\}_{20 \times 1} \langle Z_{\theta z} \rangle_{1 \times 20}^T \\
& + \{Z_{\theta z}\}_{20 \times 1} \langle Z'_{ub} \rangle_{1 \times 20}^T] dz + \langle M_{xsp} \rangle_{1 \times 2} \{Z_p\}_{2 \times 1} \{ \{Z'_{ub}\}_{20 \times 1} \langle Z_{\theta z} \rangle_{1 \times 20}^T + \{Z_{\theta z}\}_{20 \times 1} \langle Z'_{ub} \rangle_{1 \times 20}^T] dz \\
& + \int_0^L \left[\langle N_{1p} \rangle_{1 \times 2} \{Z_p\}_{2 \times 1} \left\{ \{Z'_{u1b}\}_{20 \times 1} \langle Z'_{u1b} \rangle_{1 \times 20}^T + \frac{b^2}{12} \{Z_{\theta z}\}_{20 \times 1} \langle Z_{\theta z} \rangle_{1 \times 20}^T \right\} \right] dz \\
& + \int_0^L \left[\langle N_{2p} \rangle_{1 \times 2} \{Z_p\}_{2 \times 1} \left\{ \{Z'_{u2b}\}_{20 \times 1} \langle Z'_{u2b} \rangle_{1 \times 20}^T + \frac{b^2}{12} \{Z_{\theta z}\}_{20 \times 1} \langle Z_{\theta z} \rangle_{1 \times 20}^T \right\} \right] dz \\
& - q_y(z) y_{q_y}(z) \{Z_{\theta z}\}_{20 \times 1} \langle Z_{\theta z} \rangle_{1 \times 20}^T] dz - \sum_{z_i=0,L} P_y y_p^{(z_i)} \{Z_{\theta z}^{(z_i)}\}_{20 \times 1} \langle Z_{\theta z}^{(z_i)} \rangle_{1 \times 20}^T.
\end{aligned} \tag{41}$$

The FE formulation developed in Eq. (4) is applied for the buckling analysis of the general case (*i.e.*, a steel element bonded with two GFRP laminates, as defined in Figure 1a and b). By simplifying the general case, other FE formulations can be developed for the buckling prediction of possible strengthening scenarios (*i.e.*, a bare steel beam not strengthened, a steel element bonded with a top GFRP laminate, and a steel element bonded with a bottom GFRP laminate).

4 Validation and discussion of results

Four examples are conducted to validate the FE formulation of the present study. Examples 1 and 2 validate the buckling loads and modes of single/continuous-span steel beams bonded with FRP layers predicted by the present FE formulation against those of the 3-dimensional FE analyses (3D FEA). Examples 3

and 4 compare the buckling responses of continuous bare steel beams as obtained from the present FE formulations against those obtained from previous numerical results by Sahraei *et al.* [36] and Barsoum and Gallagher [37], experiment-based approximations by Zhao and Ding [38], typical design standards for steel structures [33–35] and the 3D FEA solutions. Parametric studies in Examples 1 and 2 are also conducted to investigate the strengthening effectiveness for the LTB resistances in the FRP-bonded steel beams.

4.1 Example 1: Validation of the present solutions for a single span steel beam partially bonded with orthotropic FRP layers and parametric studies

A single-span steel beam partially bonded with two FRP layers is considered in the present example (Figure 4a and b). The beam is vertically supported by a pin support at beam end A and a movable support at beam end B (Figure 4a). Also, lateral braces in the X -axis direction are applied to the beam ends to restrain twisting angle and lateral displacements at the end cross-sections. However, the slopes of the twisting angle and lateral displacements are free at the cross-sections. The beam is subjected to a midspan point load P applied at the steel section centroid. The steel cross-section is $W250 \times 45$ ($h = 266$ mm, $b = 148$ mm, $t_f = 13$ mm, $t_w = 7.6$ mm) (Figure 4c). The thickness of both FRP layers is taken as $t_{g1} = t_{g2} = 20$ mm, while that of both epoxy bonding layers is given as $t_{a1} = t_{a2} = 1.0$ mm. The steel has a modulus of elasticity of 200 GPa and a Poisson's ratio of 0.3. The epoxy has a modulus of elasticity of 3.18 GPa and a Poisson's ratio of 0.25. The FRP layer is stacked by 16 orthotropic laminae (GF600 material [20]). Each lamina has a longitudinal elasticity modulus of $E_{k,z} = 36.87$ GPa, elastic moduli of $E_{k,s} = E_{k,n} = 10.64$ GPa, shearing stiffnesses of $G_{k,sn} = G_{k,zn} =$

3.27 GPa, $G_{k,sz} = 3.93$ GPa, and Poisson ratios of $\mu_{k,sn} = \mu_{k,zn} = 0.28$, $\mu_{k,sz} = 0.33$. The FRP laminae are symmetrically arranged by an order of $(i/-i/i/-i/i/-i/-i)_s$ where i takes a value from 0 to 90° . Three strengthening schemes are considered in the example. In the first scheme, the steel beam is bonded with the FRP layers over the whole span length (*i.e.*, $L_r = 5.0$ m, $a = 0.0$ m). In the second and third schemes, parts of the steel span are bonded with the FRP layers (*i.e.*, $L_r = 4.0$ m, $a = 0.5$ m and $L_r = 3.0$ m, $a = 1.0$ m). The buckling responses of the present study are based on the FE formulation developed in Eq. (39). The results of the buckling solutions based on the present solution are compared against those of the 3D FEA solutions conducted in ABAQUS. The effect of stacking angles and the length of FRP layers on the buckling solutions are investigated in the present example.

4.1.1 3D FEA solution

The 3D FEA solution is conducted in ABAQUS. Such solutions are based on three-dimensional FEs C3D8R in the ABAQUS library. The element has a brick shape with 8 nodes; each node has 3 nodal displacements, and 11 independent numbers of elements n_i , $i = 1, 2, \dots, 11$, are proposed for the modelling (Figure 5). Here, $n_1, n_2, n_3, n_4, n_5, n_6, n_7$, and n_8 are, respectively, the number of elements along a half of the clear flange width, the thickness of the bottom FRP layer, the thickness of the bottom epoxy layer, the flange thicknesses, the clear web height, the web thickness, the thickness of the top epoxy layer, and the thickness of the top FRP layer (Figure 5a), n_9 or n_{11} is the number of elements along each unstrengthened segments, while n_{10} is the number of elements along the strengthened segment (Figure 5b and c).

The boundary conditions at the beam ends in the 3D FEA solution are presented in Figure 6a and b, in which the pin support at beam end A can be created by restraining

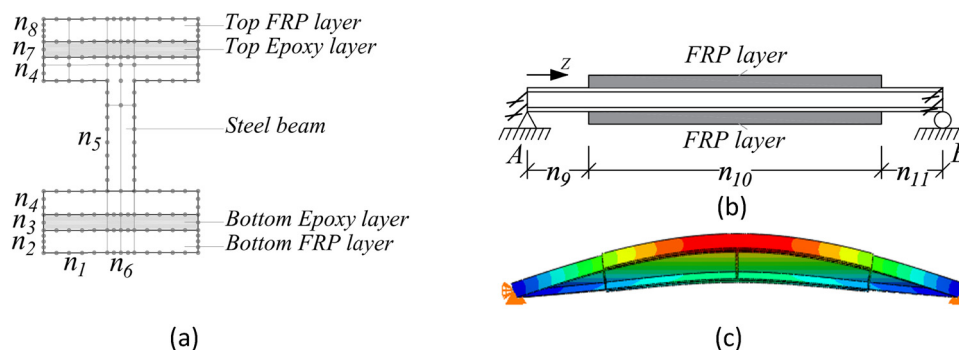


Figure 5: A 3D FEA mesh controlled by 11 independent element numbers across different edges of the model: (a) cross-section, (b) profile, and (c) the first buckling mode.

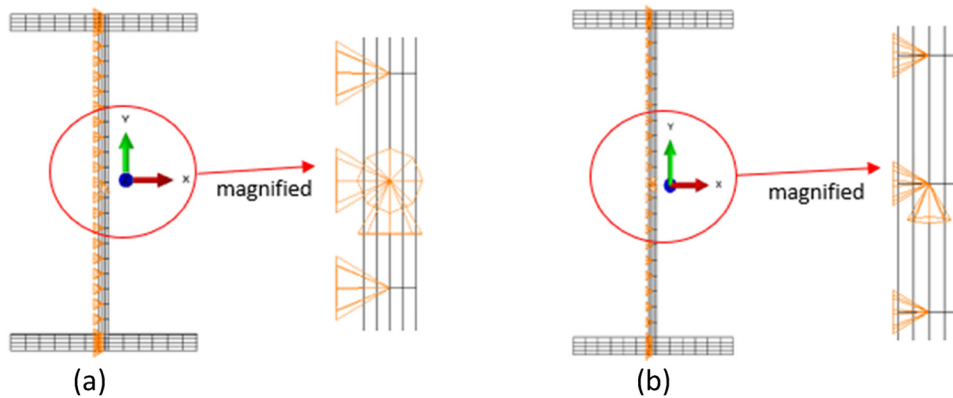


Figure 6: Boundary conditions at the left end A (a) and at the right end B (b) of the single steel beam.

the longitudinal and vertical displacements at the node coincident with the centroid of the steel cross-section with coordinate $Z = 0$ (Figure 6a). The movable support at the beam end B can be created by restraining the vertical displacement at the node coincident with the centroid of the steel cross-section with coordinate $Z = L_r + 2a$ (Figure 6b). The lateral braces can be created by restraining the lateral displacements of the nodes lying on the vertically symmetric axis of the steel cross-sections at the beam ends (Figure 6). The twisting angle and lateral displacement at the braces can be thus restrained, while their slopes are free.

A mesh study is conducted to obtain the convergence of the LTB loads based on the 3D FEA solutions. The mesh study is presented for the structure with $L_r = 4.0$ m, $a = 0.5$ m and with FRP laminae symmetrically arranged at $\pm 45^\circ$. Four meshes with different number of elements named as Meshes M1, M2, M3, and M4 are assumed and presented in Table 1.

Table 2 presents the comparison of the LTB resistances of the 3D FEA solutions based on the different meshes. As observed, the buckling load of Mesh M1 is 345.4 kN, that of Mesh M2 is 226.5 kN, that of Mesh M3 is 220.5 kN, and that of Mesh 4 is 219.9 kN. When compared to the buckling load of Mesh M4, that of Mesh M1 is 57.1% higher, that of Mesh M2 is 226.5% higher, and that of Mesh M3 is only 0.3% higher. This indicates that the buckling loads based on Mesh M3

are converged. Therefore, the 3D FEA solutions will be based on Mesh M3 for further investigations in the present example. The time for a run of Mesh 3 is 2,280 s simulated on a computer with Intel(R) and Core(TM) i7 processors and a 16 GB RAM.

4.1.2 Present solution

A mesh convergence study based on the FE formulation developed in Eq. (39) of the present study is also conducted. The present FE formulation is established by using one-dimensional elements and it does not relate to the modeling of the cross-sectional dimensions, as must be done in the 3D FEA solutions. To mesh the composite FRP-bonded steel beams, it only requires three number of elements n_9 , n_{10} , n_{11} (as defined in Figure 5b). Four different

Table 2: Buckling loads (kN) based on different meshes in the 3D FEA solution

Mesh	3D FEA solution	% difference
M1	345.4	57.1
M2	226.5	3.0
M3	220.5	0.3
M4	219.9	0.0

Table 1: Assumed 3D FEA meshes conducted in ABAQUS modeling

Mesh	n_1	n_2	n_3	n_4	n_5	n_6	n_7	n_8	n_9	n_{10}	n_{11}
M1	4	4	2	2	20	2	2	4	10	40	10
M2	10	8	4	4	40	4	4	8	20	80	20
M3	10	16	4	4	40	4	4	16	40	160	40
M4	10	16	4	4	80	4	4	16	80	320	80

Table 3: Assumed meshes in the present FE solution

Mesh	n_9	n_{10}	n_{11}
1	2	20	2
2	4	40	4
3	10	60	10
4	20	80	20

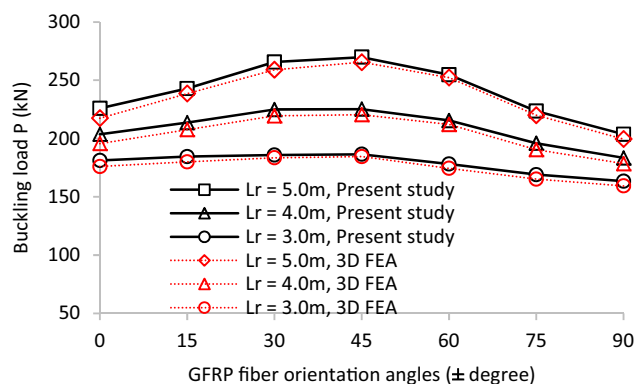
Table 4: Buckling loads based on different meshes in the present solution

Load position	Present study	% difference
Mesh 1	306.1	36.4
Mesh 2	231.7	3.2
Mesh 3	225.3	0.4
Mesh 4	224.5	0.0

Mesheres 1–4 are assumed for the mesh study, as presented in Table 3.

In the present FE formulation, the pin support at beam end A can be created by setting the governing displacements $V_p(z=0)=0$, $W_p(z=0)=0$. Also, the movable support at beam end B is created by setting the governing displacement $V_p(z=L_r+2a)=0$. The lateral braces at the beam ends can be created by setting the twisting angle and the lateral displacements $U_b(z=0)=0$, $U_b(z=L_r+2a)=0$, $\theta_{zb}(z=0)=0$, $\theta_{zb}(z=L_r+2a)=0$.

A comparison of the buckling resistances based on the different meshes of the present FE solutions is presented in Table 4. It is observed that the buckling loads are converted in the solutions using Mesheres 3 and 4. Therefore, the present study uses Mesh 3 for further investigations in the present example. The time for a run with Mesh 3 consumes about 76 s conducted in the same computer as that simulates the 3D FEA solution. It can be observed that the running time and effort for a buckling solution of the present solution are much lower than those of the three-dimensional FE analyses conducted in ABAQUS. It is noticed that the present FE formulation has been developed as a one-dimensional beam element.

**Figure 7:** Comparisons of the LTB resistance loads with different FRP fiber orientation angles predicted by the 3D FEA and the present solutions.

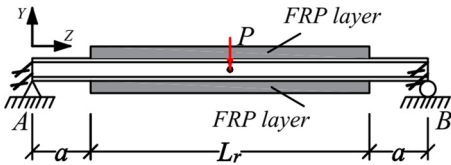
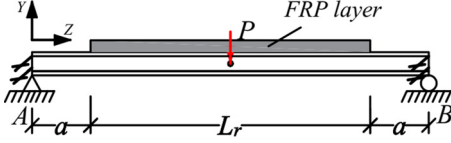
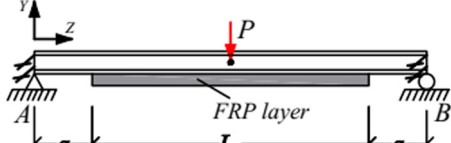
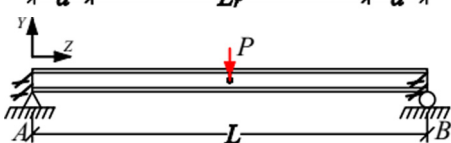
4.1.3 Results and discussion

Figure 7 presents the comparisons of the LTB resistances of the systems with different FRP fiber orientation angles for three strengthening schemes (*i.e.*, $L_r = 5.0$ m, $L_r = 4.0$ m, or $L_r = 3.0$ m) predicted by the 3D FEA and the present solutions. For each scheme, the buckling loads obtained from the present FE solution are in an excellent agreement with those of the 3D FEA solution. For example, in the scheme $L_r = 5.0$ m and fiber angles of 0° , the buckling load of the present solution is 225.9 kN, while that of the 3D FEA solution is 217.5 kN, corresponding to a difference of 3.9%. In the scheme $L_r = 4.0$ m and fiber angles of 0° , the buckling load of the present solution is 203.6 kN, while that of the 3D FEA solution is 195.7 kN, a difference of 4.0%. For the scheme $L_r = 3.0$ m and fiber angles of 0° , the buckling load predicted by the present solution is 181.2 kN, while that of the 3D FEA solution is 176.0 kN, a difference of 3.0%. Excellent agreements of the buckling loads for the systems with fiber angles from 15° to 90° are also observed between the two solutions.

Based on the present solution in Figure 6, two important effects of the FRP layers on the LTB resistances of the steel beams strengthened with FRP are observed. First, the systems with FRP lamina angles oriented at $\pm 45^\circ$ have the maximum buckling loads, while those oriented at $\pm 90^\circ$ have the smallest buckling loads. This can be explained as follows: the FRP layers with fiber orientation arrangements $\pm 45^\circ$ may maximize \bar{Q}_{66} , and the torsional and shear stiffnesses (*i.e.*, $\bar{A}_{g1,66}b_1$ and $b_1\bar{D}_{g1,66}$, respectively) of the FRP layer (Appendix 1). The observation and results of the present study are consistent with several previous solutions (*e.g.*, [11–20]). Second, the strengthening length of FRP layers also has a significant effect on the buckling loads of the systems. For example, the system with fiber angles of 0° , the buckling load of the strengthening scheme $L_r = 5.0$ m is 225.9 kN, while that of scheme $L_r = 3.0$ m is 181.2, a difference of up to 19.8%. For the system with fiber angles of $\pm 45^\circ$, the buckling load of the strengthening scheme $L_r = 5.0$ m is 269.9 kN, while that of scheme $L_r = 3.0$ m is 186.5 kN, a difference of 30.9%. For each of the fiber angles from 0° to 90° , the LTB resistances of the system with different strengthening lengths $L_r = 5.0$ m, $L_r = 4.0$ m, $L_r = 3.0$ m are highly different, as observed in Figure 7. This indicates that the buckling resistance of the FRP-strengthened steel beams significantly depends on the strengthening length of the FRP layers.

Based on the present solution, the strengthening effectiveness of using FRP layers can be quantified. The LTB resistance of the bare beam (without strengthening) is

Table 5: Comparisons of the LTB resistance predicted by the 3D FEA and the present solutions in four other strengthening schemes in Example 1

Other strengthening scenarios	Description in figure	FRP stacking angles	Buckling load P (kN)		% difference
			Present study	3D FEA solution	
(1)	(2)	(3)	(4)	(5)	(4-5)/(5)
1st		0°	225.9	217.5	3.9
2nd		0°	172.2	167	3.1
3rd		0°	192.4	187	2.9
4th		Not applicable	136.9	135.2	1.3

136.9 kN (Table 5). For the FRP layers with fiber angles of 0°, the LTB resistance of the steel beams bonded with a 5.0 m-long FRP layer is 225.9 kN, corresponding to the effectiveness of 39.4%, while the LTB resistance of the steel beams bonded with a 3.0 m-long FRP layer is 181.2 kN, corresponding to the effectiveness of 24.5%. For FRP layers with fiber angles of ±45°, the LTB resistance of the steel beams strengthened with a 5.0 m-long FRP layer is 269.9 kN, corresponding to the effectiveness of 49.5%, while the LTB resistance of the steel beams bonded with a 3.0m-long FRP layer is 186.5 kN, corresponding to the effectiveness of 26.6%. In this example, the FRP strengthening effectiveness is dependent on both the strengthening length and the orthotropic properties of the FRP layers.

4.1.4 Further validations of the present solution for the buckling load predictions of the steel beams in four other strengthening scenarios

Four other systems are considered: the first strengthening scenario is for the steel beam bonded with two FRP layers, the second and third scenarios are for that strengthened

with a top or bottom FRP layer and the last one is for a bare beam. The length of FRP layers in the four strengthening scenarios are taken as $L_r = L = 5.0$ m, $a = 0$, while the FRP layers are stacked by 0° angles. The mechanical properties and thickness of the FRP layers are given in Example 1. The buckling resistances of the present study are based on the FE formulations presented in Eq. (39) with minimized non-existing parameters. A 3D FEA solution is again adopted to validate the present study.

In Table 5, the LTB resistance differences of the four strengthening scenarios predicted by the 3D FEA and the present solutions are only from 1.3 to 3.9%. This implies that the buckling predictions of the present study are in good agreement with those of the 3D FEA solutions. Based on the present study, the effectiveness of FRP strengthening can be evaluated. By comparing to the LTB resistance of the bare beam (*i.e.*, 136.9 kN, based on the fourth scenario), the LTB resistance of the beam bonded with two FRP layers (*i.e.*, 225.9 kN in the first strengthening scenario) is 39.4% higher, that of the beam bonded with a top FRP layer (*i.e.*, 172.2 kN in the second strengthening scenario) is 25.8% higher, and that of the beam bonded with a bottom FRP layer (that is, 192.4 kN in the third strengthening scenario) is 40.5% higher.

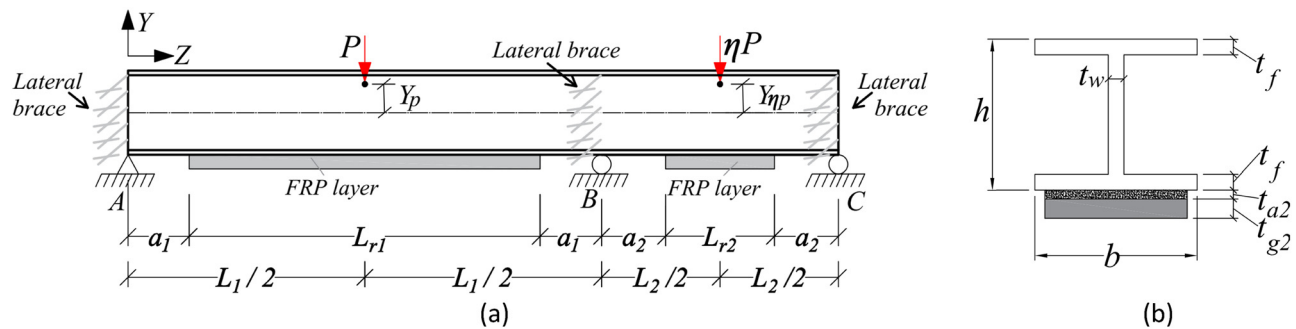


Figure 8: Profile (a) and cross-section (b) of the two-span continuous composite beam in Example 3.

4.2 Example 2: Validation of the present solutions for LTB predictions of continuous FRP-bonded steel beams under the effect of different load height positions

A two-span steel beam of Zhao and Ding [38] is visited in the present example, and is presented in Figure 8. The beam has a vertical pin support at Point A and movable supports at Points B and C. Lateral braces are applied to Points A, B, and C to restrain the lateral displacement and twisting angle at these cross-sections. The beam has a cross-section with dimensions $h = 300$ mm, $b = 200$ mm, $t_w = 10$ mm, and $t_f = 16$ mm. Span L_1 is taken as, 5.0 m while the ratio L_2/L_1 is taken as 0.5. In the present example, span L_1 is bonded with a GFRP laminate with a length of $L_{r1} = 4.6$ m, while span L_2 is bonded with another GFRP laminate with a length of $L_{r2} = 2.1$ m. Both of the FRP layers are made by stacking 16 equally thick orthotropic GF800 laminae [18] oriented at fiber angles of 0° . The laminae have an axial, lateral, and transverse moduli of elasticity of $E_{k,z} = 45.95$ GPa, $E_{k,s} = E_{k,n} = 14.56$ GPa, shearing stiffnesses of $G_{k,sn} = G_{k,zn} = 5.51$ GPa, $G_{k,sz} = 5.51$ GPa, and Poisson's ratios of $\mu_{k,sn} = \mu_{k,zn} = 0.3$, $\mu_{k,sz} = 0.33$. The steel has an elasticity modulus of 200 GPa and a Poisson ratio of 0.3. Steel has an elasticity modulus of 3.18 GPa and a Poisson ratio of 0.3. Loads P and ηP (where $\eta = 1.0$) are assumed to be applied to the top flange centroid, steel section centroid, or bottom flange centroids to account for the effect of load height positions. The LTB resistances obtained by the present FE solution are validated with the 3D FEA solutions.

4.2.1 Result discussion

Table 6 compares the LTB resistances as obtained from the 3D FEA and the present solutions for different load-high positions of P . When the load is applied at the top flange centroid, the LTB resistance obtained by the present study is 474.2 kN,

while that of the 3D FEA solution is 471.3 kN, a difference of 0.6%. Also, the differences between the two solutions are only 0.3 and 0.5% when the loads are applied at the steel section centroid and bottom flange centroid, respectively.

Figure 9 compares the LTB mode shapes (i.e., U_b , θ_{yb} , θ_{zb} , ψ_b , U_{2b} and θ_{y2b}) as predicted by the 3D FEA and the present solutions when loads P and ηP are applied at the steel section centroid. The mode shapes predicted by the two solutions can be observed to be in excellent agreement. This indicates that the LTB responses of the 3D FEA solution can be exactly captured by the present solution. In Figure 9, it can also be observed that the slope of U_b , the magnitude of θ_{yb} , the slope of θ_{zb} , the magnitude of ψ_b at Support A are generally higher than those at the middle support (i.e., Support B of Span L_1). This reflects that there is an interaction between the two spans (i.e., spans L_1 and L_2) at the middle support.

4.3 Example 3: Validation of the present solution against the standard guide-based solutions and non-shear deformable theory-based FE solutions for the buckling prediction of continuous bare steel beams

The present typical design standards (e.g., AISC [33], CSA [34], and AUS [35]) do not provide simplified equations for

Table 6: A comparison of the LTB resistances (kN) obtained from the 3D FEA and the present solutions under the effect of load height positions

Load position	Present solution	3D FEA solution	% difference
Top flange centroid	474.2	471.3	0.6
Section centroid	816.7	814.2	0.3
Bottom flange centroid	1379.0	1372.4	0.5

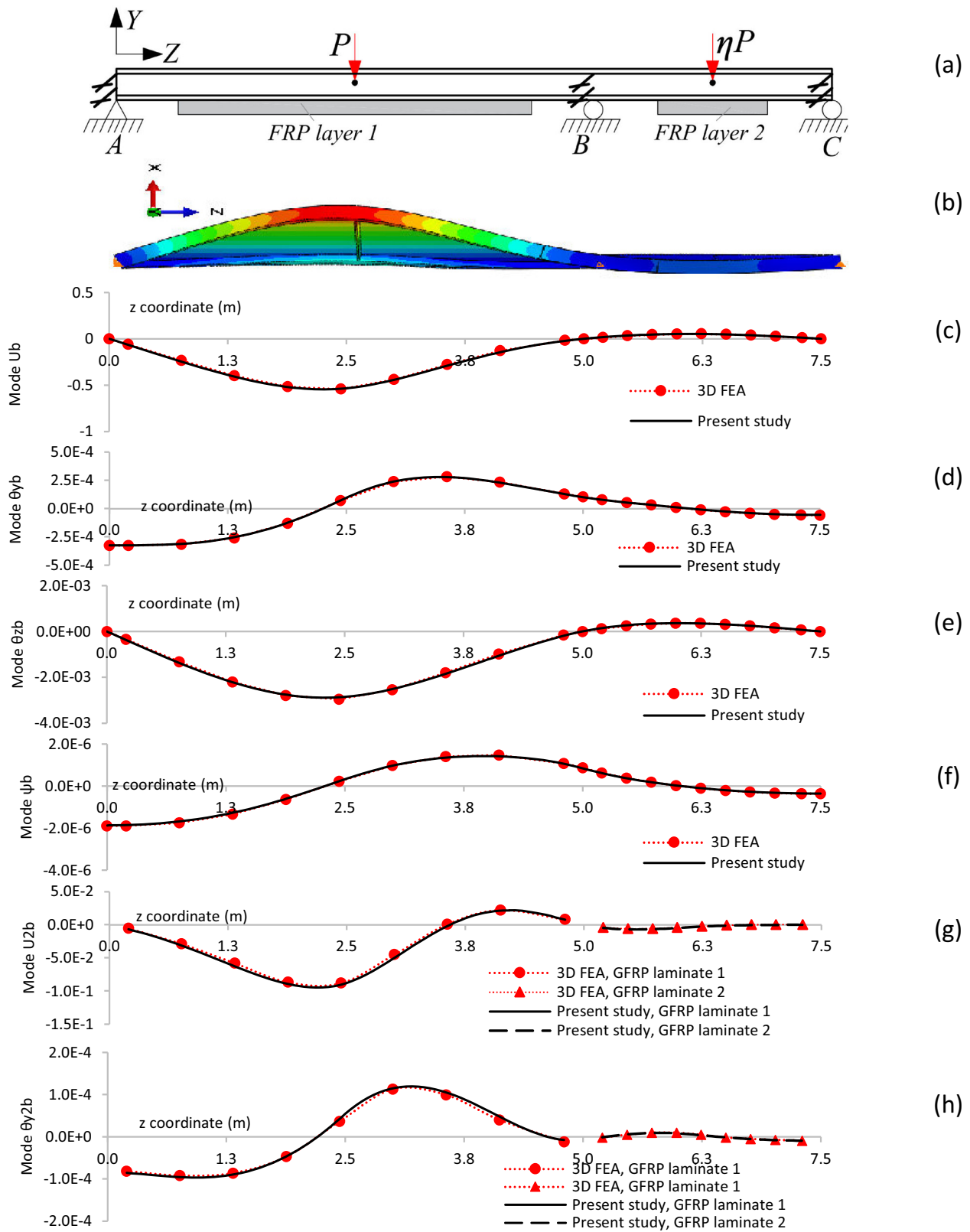


Figure 9: Comparison of buckling modes obtained from the 3D FEA and the present solutions; (a) Beam profile, (b) 3D FEA buckling configuration, and (c–h) buckling modes.

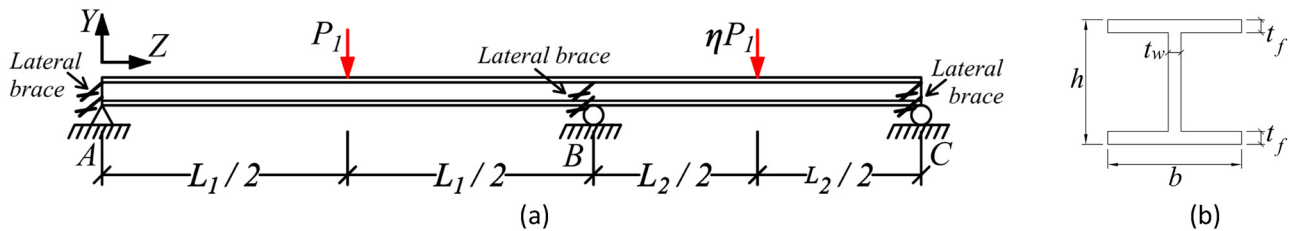


Figure 10: Profile (a) and cross-section (b) of the two-span continuous steel beam in Example 3.

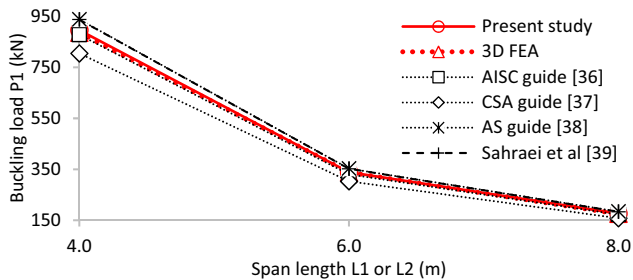


Figure 11: Comparisons of the buckling resistances obtained from different solutions for different spans.

the elastic LTB loads of continuous beams. In order to approximately evaluate the buckling load, engineers often treat each unbraced segment as a separate span, then to calculate the individual LTB resistance of each segment separately, and to conservatively use the smallest critical moment as the one governing the LTB resistance of the continuous beam. Such a treatment may ignore the span interaction in continuous beams, as suggested by Sahraei *et al.* [36]. However, the solution of Sahraei *et al.* [36] followed a non-shear FE formulation of Barsoum and Gallagher [37], *i.e.*, the shear deformation effects were not captured in these investigations. Thus, this example will validate the buckling loads predicted by the present shear FE formulations developed in Eq. (40) against those of the standard guides [33–35] and the non-shear FE formulation [36].

A two-span bare steel beam is considered, as presented in Figure 10a and b. The length of the first span is L_1 while that of the second span is L_2 . The beam has a vertical pin and movable supports at Points A, B, and C. Lateral braces are applied to the points to restrain the lateral displacement and twisting angle of these cross-sections. The steel cross-sectional dimensions are h , b , t_f , and t_w . The left span is under a midspan load of P_1 while the right one is under another load ηP_1 , where η is a real number.

Sahraei *et al.* [36] adopted the non-shear deformable FE formulation developed by Barsoum and Gallagher [37] for the buckling load predictions of the two-span beam in Figure 10a and b, in which the beam has a cross-section of $W250 \times 58$ ($h = 252$ mm, $b = 203$ mm, $t_w = 8.0$ mm, and

$t_f = 13.5$ mm) and an elasticity modulus of 200 GPa. Span lengths $L_1 = L_2$, where L_1 are 4.0, 6.0, or 8.0 m. The load factor η is equal to 1.0 and both loads P_1 and ηP_1 are applied to the centroids of the steel beam cross-sections. Figure 10 presents the comparisons of the buckling loads P_1 of different span lengths $L_1 = L_2 = 4.0, 6.0, 8.0$ m as obtained from the present solution, Sahraei *et al.* [36], AISC standard guide [33], Canadian standard CSA guide [34], Australia standard guide [35], and the present 3D FEA. Among the solutions, the buckling resistances of the 3D FEA solution are considered as the reference solutions to compare against the others. The buckling load of the beam with span $L_1 = L_2 = 4.0$ m predicted by the present FE solution is 895.7 kN, while that based on the 3D FEA solution is 885.5 kN, corresponding to a difference of 1.2%. For spans $L_1 = L_2 = 6.0$ m and $L_1 = L_2 = 8.0$ m, the differences between the two solutions are 0.2 and 0.6%, respectively (Figure 11). This indicates that the buckling loads predicted by the present solution excellently agree with those of the 3D FEA solution.

The LTB loads predicted by Sahraei *et al.* [36] are higher than those based on the 3D FEA solutions (Figure 11). For span $L_1 = L_2 = 4.0$ m, the LTB load based on Sahraei *et al.* [36] is 937.4 kN, which is 5.9% higher than the 3D FEA buckling load. For spans $L_1 = L_2 = 6.0$ m and $L_1 = L_2 = 8.0$ m, Sahraei *et al.* [36] predicted the LTB loads, those are, respectively, 4.1 and 4.9% higher than the 3D FEA buckling loads. The over-prediction of the solutions by Sahraei *et al.* [36] may originate from the shear deformation neglect in their Barsoum and Gallagher FE solutions [37]. In contrast, the present study considers the contribution of shear deformations and thus better agrees with the 3D FEA solution for the LTB prediction.

From AISC, CSA, and AUS standard guides [33–35], the LTB loads of the two-span beam are evaluated and presented in Figure 11. For span $L_1 = L_2 = 4.0$ m, the LTB loads of AISC, CSA, and AUS guides are 877.9, 804.2, and 938.0 kN, respectively, and those are 0.9, 9.2, and 5.9% different from the LTB loads of the 3D FEA. The differences are, respectively, 2.3, 10.5, and 4.4% for span $L_1 = L_2 = 6.0$ m and 1.4, 9.7, and 5.3% for span $L_1 = L_2 = 8.0$ m. Among the solutions considered, the present FE solutions most agree with the 3D FEA and the AISC solutions. Also,

Table 7: Comparisons of the buckling resistances obtained from different solutions for different span ratios

Span ratio L_2/L_1	Solutions of buckling load P_1 (kN)			Comparison of the solutions against the 3D FEA solution (%)	
	Present solution	Zhao and Ding [38]	3D FEA solution		
(1)	(2)	(3)	(4)	$ 2-4 /(4)$	$ 3-4 /(4)$
0.5	444.8	443.4	439.6	1.2	0.9
0.6	438.1	435.4	432.5	1.3	0.7
0.7	431.8	429.4	426.8	1.2	0.6
0.8	423.5	419.4	418.2	1.3	0.3
0.9	408.9	395.5	403.6	1.3	2.0
1.0	379.6	359.5	372.1	2.0	3.4

the solutions based on CSA and AUS standards are considerably different from the 3D FEA solutions.

4.4 Example 4: Validations of the present solution against the experimental solutions of Zhao and Ding [38] and the 3D FEA solutions for the buckling load of the continuous beams

Zhao and Ding [38] reported experimental results on the LTB of two-span steel beams (Figure 9a and b). They proposed an approximation equation for the evaluation of the elastic LTB solution of the continuous beams. A 3D FEA solution in ABAQUS is conducted in the present example to compare against both solutions. A two-span beam studied in Zhao and Ding [38] (Figure 10a and b) is visited in the present example, in which the beam has a cross-section with dimensions $h = 300$ mm, $b = 200$ mm, $t_w = 10$ mm, and $t_f = 16$ mm. Loads P_1 and ηP_1 (where $\eta = 1.0$) are applied on the top flange position. Span L_1 is 5.0 m while ratios L_2/L_1 are taken as 0.5, 0.6, 0.7, 0.8, 0.9, or 1.0.

Table 7 compares the buckling loads P_1 for different span ratios L_2/L_1 , as predicted by the solutions of Zhao and Ding [38], the 3D FEA, and the present study. As observed, the differences in the buckling loads between the three solutions are from 0.3 to 3.4%. This indicates that the present solution again agrees with the 3D FEA solution and the solution by Zhao and Ding [38]. Based on Table 7, it can also be observed that the buckling load of the continuous beam is smaller when the span ratio L_2/L_1 increases.

5 Conclusions

The present study successfully developed a beam-based FE formulation for the LTB analyses of steel beams partially

bonded with orthotropic FRP layers. The effects of partial interactions between different materials, local and global warping deformations, and load height positions were also captured in the solutions. To develop the FE formulation, a shear deformable theory was first proposed to describe the buckling equilibrium states of the system, in which the buckling equilibrium state was described by eight out-of-plane governing displacement fields. Strains and stresses were then derived and the total buckling potential energy of the system was expressed in terms of the governing displacements. An FE formulation based on linear and cubic shape functions was then developed. Such an element had two nodes and each node had ten degrees of freedom. Through the comparisons of the buckling responses of various single and continuous span systems obtained from the present solution against previous experimental and numerical results, design standard guides of steel structures and the 3D FEA solutions conducted in ABAQUS, key conclusions were obtained as follows.

The buckling loads/modes of the single and continuous beams predicted by the present solution excellently agree with those of previous experimental/numerical studies, as observed in Examples 1–4.

Based on Examples 1 and 2, it was also observed that the steel beams strengthened with FRP lamina angles oriented at $\pm 45^\circ$ had the highest buckling loads, while those oriented at $\pm 90^\circ$ had the smallest buckling loads. Also, the strengthening length of FRP layers had a significant effect on the buckling loads of the FRP-strengthened steel beams. This was reported in Example 1 in which the buckling loads of a 5 m span steel beam bonded with 5 m long FRP layers were 19.8 to 30.9% higher than those bonded with 3 m long FRP layers.

As observed in Examples 3 and 4, the effects of shear deformations were captured in the 3D FEA and the present solutions. The buckling loads of such solutions were smaller than those predicted by non-shear deformable FE solutions. Also, the present solution and the 3D FEA

solution captured the effect of span interactions in continuous beams and were not considered in several design standards of steel structures.

The FRP strengthening effectiveness for the LTB loads of the steel beams was from 24.5 to 49.5%, as observed in Examples 1 and 2.

Funding information: This research was supported by the Vietnam Ministry of Education and Training, Project B2023-GHA-06.

Author contributions: All authors have accepted responsibility for the entire content of this manuscript and provided consent to its submission to the journal, reviewed all the results and approved the final version of the manuscript. TD-T, X-HN, and PVP contributed equally as main contributors of this article. TD-T: investigation, FE formulation, writing, drawing, validation, and parametric studies; X-HN: conceptualization, writing and editing; validation, and parametric studies; PVP: methodology, FE formulation, writing, editing, validation, and parametric studies.

Conflict of interest: The authors state no conflict of interest.

References

- [1] Miller CT, Chajes JM, Hastings NJ. Strengthening of a steel bridge girder using CFRP plates. *J Bridge Eng.* 2001;6(6):514–22.
- [2] Zhao XL, Zhang L. State-of-the-art review on FRP strengthened steel structures. *Eng Struct.* 2007;29(8):1808–23.
- [3] Harries AK, El-Tawil S. Steel-FRP composite structural systems. *Int. Conf. on Composite Construction in Steel and Concrete 2008*, Composite Construction in Steel and Concrete VI. Reston, VA: ASCE; 2008. p. 703–16.
- [4] Fam A, Mac D, Shaat A. Upgrading steel-concrete composite girders and repair of damaged steel beams using bonded CFRP laminates. *Thin-Walled Struct.* 2009;47(10):1122–35.
- [5] El Damatty AA, Abushagur M. Testing and modeling of shear and peel behavior for bonded steel/FRP connections. *Thin-Walled Struct.* 2003;41(11):987–1003.
- [6] El Damatty A, Abushagur M, Youssef MA. Experimental and analytical investigation of steel beams rehabilitated using GFRP sheets. *J Steel Compos Struct.* 2003;3(6):421–38.
- [7] Accord NB, Earls CJ. Use of fiber-reinforced polymer composite elements to enhance structural steel member ductility. *J Compos Constr.* 2006;10(4):337–44.
- [8] Aguilera J, Fam A. Bonded FRP. Plates for strengthening rectangular hollow steel section T-joints against web buckling induced by transverse compression. *J Compos Constr ASCE.* 2013;17(4):421–32.
- [9] Correia JR, Branco FA, Silva NMF, Camotim D, Silvestre N. First-order, buckling and post-buckling behaviour of GFRP pultruded beams. Part 1: Experimental study. *Computers Struct.* 2011;89(21–22):2052–64.
- [10] Aydin E, Aktas M. Obtaining a permanent repair by using GFRP in steel plates reformed by heat-treatment. *Thin-Walled Struct.* 2015;94:13–22.
- [11] Raj FM, Nagarajan VA, Elsi SS, Jayaram RS. Effect of fiber content on flexural properties of fishnet/GFRP hybrid composites. *Steel Compos Struct.* 2016;22(1):13–24.
- [12] Hosseini SA, Bahaari MR, Lesani M, Hajikarimi P. Static load-bearing capacity formulation for steel tubular T/Y-joints strengthened with GFRP and CFRP. *Compos Struct.* 2021;267:113950.
- [13] Lesani M, Hosseini SA, Bahaari MR. Load bearing capacity of GFRP-strengthened tubular T-joints: Experimental and numerical study. *Structures.* 2022;38:1151–64.
- [14] Siddique MAA, El Damatty AA. Enhancement of buckling capacity of steel plates strengthened with GFRP plates. *Thin-Walled Struct.* 2012;60:154–62.
- [15] Siddique MAA, El Damatty AA. Improvement of local buckling behavior of steel beams through bonding GFRP plates. *Compos Struct.* 2013;96:44–56.
- [16] Youssef M. Analytical prediction of the linear and nonlinear behaviour of steel beams rehabilitated using FRP sheets. *Eng Struct.* 2006;28(6):903–11.
- [17] Silva NMF, Camotim D, Silvestre N, Correia JR, Branco FA. First order, buckling and post buckling behaviour of GFRP pultruded beams. Part 2: Numerical simulation. *Compos Struct.* 2011;89(21–22):2065–78.
- [18] Xin H, Liu Y, Mosallam AS, He J, Du A. Evaluation on material behaviors of pultruded glass fiber reinforced polymer (GFRP) laminates. *Compos Struct.* 2017;182:283–300.
- [19] Phe PV. An innovated theory and closed form solutions for the elastic lateral torsional buckling analysis of steel beams/columns strengthened with symmetrically balanced GFRP laminates. *Eng Struct.* 2022;256:114046.
- [20] Lee J, Lee SH. Flexural-torsional behavior of thin-walled composite beams. *Thin-Walled Struct.* 2004;42(9):1293–305.
- [21] Phe PV, Mohareb M. A shear deformable theory for the analysis of steel beams reinforced with GFRP plates. *Thin-Walled Struct.* 2014;85:165–82.
- [22] Phe PV. Solutions of the interfacial shear and normal stresses in plate flexural-strengthened beams based on different complementary strain energy assumptions. *Eng Struct.* 2021;229:111567.
- [23] Linghoff D, Emrani M. Performance of steel beams strengthened with CFRP laminate – Part 2: Laboratory tests. *Compos Part B.* 2010;41(7):516–22.
- [24] Linghoff D, Emrani A, Kliger MR. Performance of steel beams strengthened with CFRP laminate – Part 1: Laboratory tests. *Compos Part B.* 2010;41(7):509–15.
- [25] Girhammar UA, Pan DH. Exact static analysis of partially composite beams and beam-columns. *Int J Mech Sci.* 2007;49(2):239–55.
- [26] Xu R, Wu Y. Static, dynamic, and buckling analysis of partial interaction composite members using Timoshenko's beam theory. *Int J Mech Sci.* 2007;49(10):1139–55.
- [27] Challamel N, Girhammar UA. Lateral-torsional buckling of vertically layered composite beams with interlayer slip under uniform moment. *Eng Struct.* 2012;34:505–13.
- [28] Schnabl S, Planinc I. Inelastic buckling of two-layer composite columns with nonlinear interface compliance. *Int J Mech Sci.* 2011;53(12):1077–83.
- [29] Kabir MZ, Seif AE. Lateral-torsional buckling of retrofitted steel I-beams using FRP sheets. *Int J Sci Tech Trans A: Civ Eng.* 2010;17(4):262–72.

- [30] Grogneć PL, Nguyen QH, Hjić M. Exact buckling solution for two-layer Timoshenko beams with interlayer slip. *Int J Solids Struct.* 2012;49(1):143–50.
- [31] Phe PV, Mohareb M, Fam A. Lateral torsional buckling analysis of steel beams strengthened with GFRP plate. *Thin-Walled Struct.* 2018;131:55–75.
- [32] Zaghian S, Mohareb M. Elastic buckling strength for steel plates symmetrically strengthened with glass fiber reinforced polymer plates. *Can J Civ Eng.* 2020;47(3):337–53.
- [33] ANSI/AISC 360-10. Specification for Structural Steel Buildings, American Institute of Steel Construction (AISC). Chicago, IL: AISC; 2010.
- [34] CAN/CSA-S16-14. Limit states design of steel structures. Ontario: Canadian Standards Association; 2014.
- [35] AS-4100 1998. AS-4100 Steel Structures, Standards Australia. Sydney, Australia: 1998.
- [36] Sahraei A, Pezeshky P, Mohareb M. Lateral torsional buckling analysis and design of steel beams with continuous spans. Conference of Leadership in Sustainable Infrastructure, Vancouver, Canada; 2017.
- [37] Barsoum RS, Gallagher RH. Finite element analysis of torsional and torsional–flexural stability problems. *Int J Numer Methods Eng.* 1970;2(3):335–52.
- [38] Zhao J, Ding W. Tests and design method on overall buckling behaviours of welded I-section two-span continuous beams for Q460 high strength steel. *Eng Struct.* 2022;253:113789.
- [39] Phe PV. Stress-deformation theories for the analysis of steel beams reinforced with GFRP plates. Master's Science Thesis. Ottawa, Canada: University of Ottawa; 2013.
- [40] Reddy JN. Mechanics of laminated composite plates and shells – Theory and analysis. 2nd edn. Boca Raton, Florida 33431: CRC Press; 2004.
- [41] Thanh BT, Phe PV. Innovated shear deformable FE formulations for the analyses of steel beams strengthened with orthotropic GFRP laminates. *Lat Am J Solids Struct.* 2023;20(4):e487.
- [42] Jones RM. Mechanics of composite materials. 2nd edn. Philadelphia, PA 19106: Taylor & Francis; 1998.
- [43] Barbero EJ. Introduction to composite materials design. 2nd edn. Boca Raton, FL 33487-2742: CRC Press, Taylor & Francis Group; 2010.
- [44] Lanczos C. The variational principles of mechanics. Toronto: University of Toronto Press; 1949.

Appendix 1 – Evaluation of GFRP laminate stiffnesses

Plane stress-reduced stiffnesses of the k th GFRP lamina (as defined in Figure 9) can be evaluated as

$$\begin{aligned} Q_{k,11} &= E_{k,z}/(1 - \nu_{zs}\nu_{sz}), & Q_{k,12} &= \nu_{zs}E_{k,s}/(1 - \nu_{zs}\nu_{sz}), \\ Q_{k,22} &= E_{k,s}/(1 - \nu_{zs}\nu_{sz}), & Q_{k,66} &= G_{k,sz}. \end{aligned} \quad (\text{A1})$$

Here, parameters $E_{k,z}$, $E_{k,s}$, $G_{k,sz}$, $\nu_{k,zs}$, $\nu_{k,sz}$ are defined in Section 3.4. The transformed lamina stiffnesses of a lamina can be evaluated as

$$\begin{aligned} \bar{Q}_{k,11} &= Q_{k,11} \cos^4 \gamma_k + 2(Q_{k,12} + 2Q_{k,66}) \sin^2 \gamma_k \cos^2 \gamma_k \\ &\quad + Q_{k,22} \sin^4 \gamma_k, \\ \bar{Q}_{k,12} &= (Q_{k,11} + Q_{k,22} - 4Q_{k,66}) \sin^2 \gamma_k \cos^2 \gamma_k \\ &\quad + Q_{k,12} (\sin^4 \gamma_k + \cos^4 \gamma_k), \\ \bar{Q}_{k,22} &= Q_{k,11} \sin^4 \gamma_k + 2(Q_{k,12} + 2Q_{k,66}) \sin^2 \gamma_k \cos^2 \gamma_k \\ &\quad + Q_{k,22} \cos^4 \gamma_k, \\ \bar{Q}_{k,16} &= (Q_{k,11} - Q_{k,12} - 2Q_{k,66}) \sin \gamma_k \cos^3 \gamma_k \\ &\quad + (Q_{k,12} - Q_{k,22} + 2Q_{k,66}) \sin^3 \gamma_k \cos \gamma_k, \\ \bar{Q}_{k,26} &= (Q_{k,11} - Q_{k,12} - 2Q_{k,66}) \sin^3 \gamma_k \cos \gamma_k \\ &\quad + (Q_{k,12} - Q_{k,22} + 2Q_{k,66}) \sin \gamma_k \cos^3 \gamma_k, \\ \bar{Q}_{k,66} &= (Q_{k,11} + Q_{k,22} - 2Q_{k,12} - 2Q_{k,66}) \sin^2 \gamma_k \cos^2 \gamma_k \\ &\quad + Q_{k,66} (\sin^4 \gamma_k + \cos^4 \gamma_k), \end{aligned} \quad (\text{A2})$$

where γ_k is the fiber orientation angle of the k th lamina. Then, the extensional and bending stiffnesses of a GFRP laminate can be obtained through

$$\begin{aligned} A_{gi,ej} &= \sum_{k=1}^n \bar{Q}_{k,ej} (\bar{y}_{k+1} - \bar{y}_k), \\ D_{gi,ej} &= \sum_{k=1}^n \bar{Q}_{k,ej} (\bar{y}_{k+1}^3 - \bar{y}_k^3)/3, \quad (e, j = 1, 2, \dots, 6). \end{aligned} \quad (\text{A3})$$

Based on Eqs. (A3), plate stiffnesses $\bar{A}_{gi,11}$, $\bar{A}_{gi,66}$, $\bar{D}_{gi,11}$, $\bar{D}_{gi,66}$ developed in Eq. (19) can be evaluated as

$$\begin{aligned} \bar{A}_{gi,11} &= A_{gi,11} - A_{gi,12}^2/A_{gi,22}, \\ \bar{A}_{gi,66} &= A_{gi,66} - A_{gi,26}^2/A_{gi,22}, \\ \bar{D}_{gi,11} &= D_{gi,11} - D_{gi,12}^2/D_{gi,22}, \\ \bar{D}_{gi,66} &= D_{gi,66} - D_{gi,26}^2/D_{gi,22}. \end{aligned} \quad (\text{A4})$$